Referee 1

Dear Referee 1,

I am very grateful to you for the valuable and useful comments and remarks! Please, find below the answers to the comments and remarks.

Kind regards, Vera on behalf of the co-authors

Section 2.2: It would be useful to include a figure of the meshes to a) see the exact location of open boundary and b) details of the mesh resolution in crucial areas (e.g. Lister Deep, shallow areas). As the grid plays an important role in such studies, the authors should elaborate on the criteria used to choose the mesh resolution

Thank you for the comment! Please, find an answer below.

The minimum grid cell size (2-14 meters) was chosen based on available bathymetry data resolution. In case of the curvilinear grid the cell sizes are determinate by the square of the subarea. The whole domain was divided into 6 subareas (Fig. 1a). The smallest among them are those, which are covered the Königshaven area and Lister zone. The division of the domain into subareas was dictated by the bathymetry information and area of particular interests - Königshaven, Lister Deep and ets. Figure 1 shows the subdivisions, grid quality and final nodal areas for the curvilinear grid.

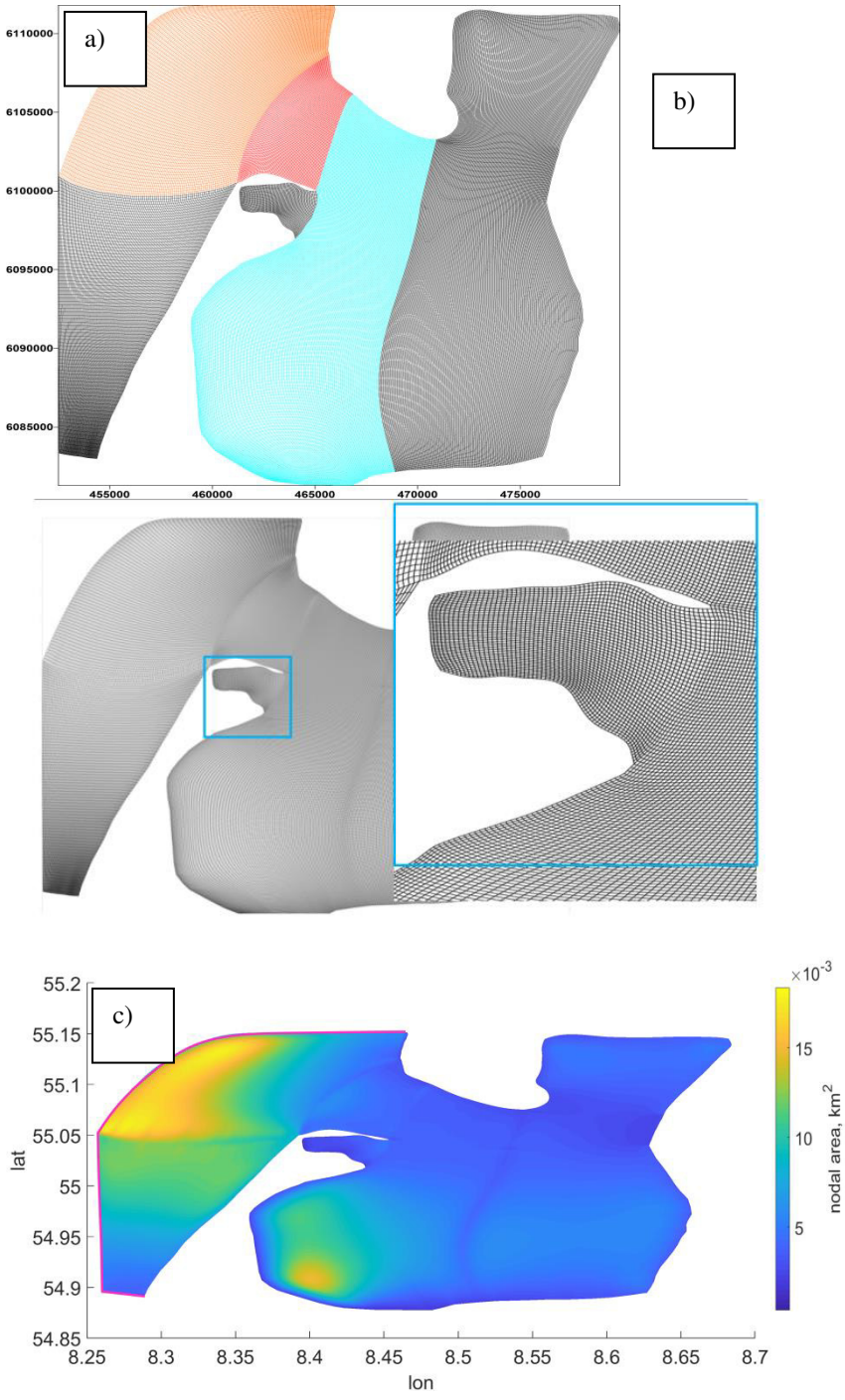

Fig. 1. Demonstration of the curvilinear grid: a) subdivision into subareas; b) grid quality; c) nodal area, pink color indicates open boundary position.

20

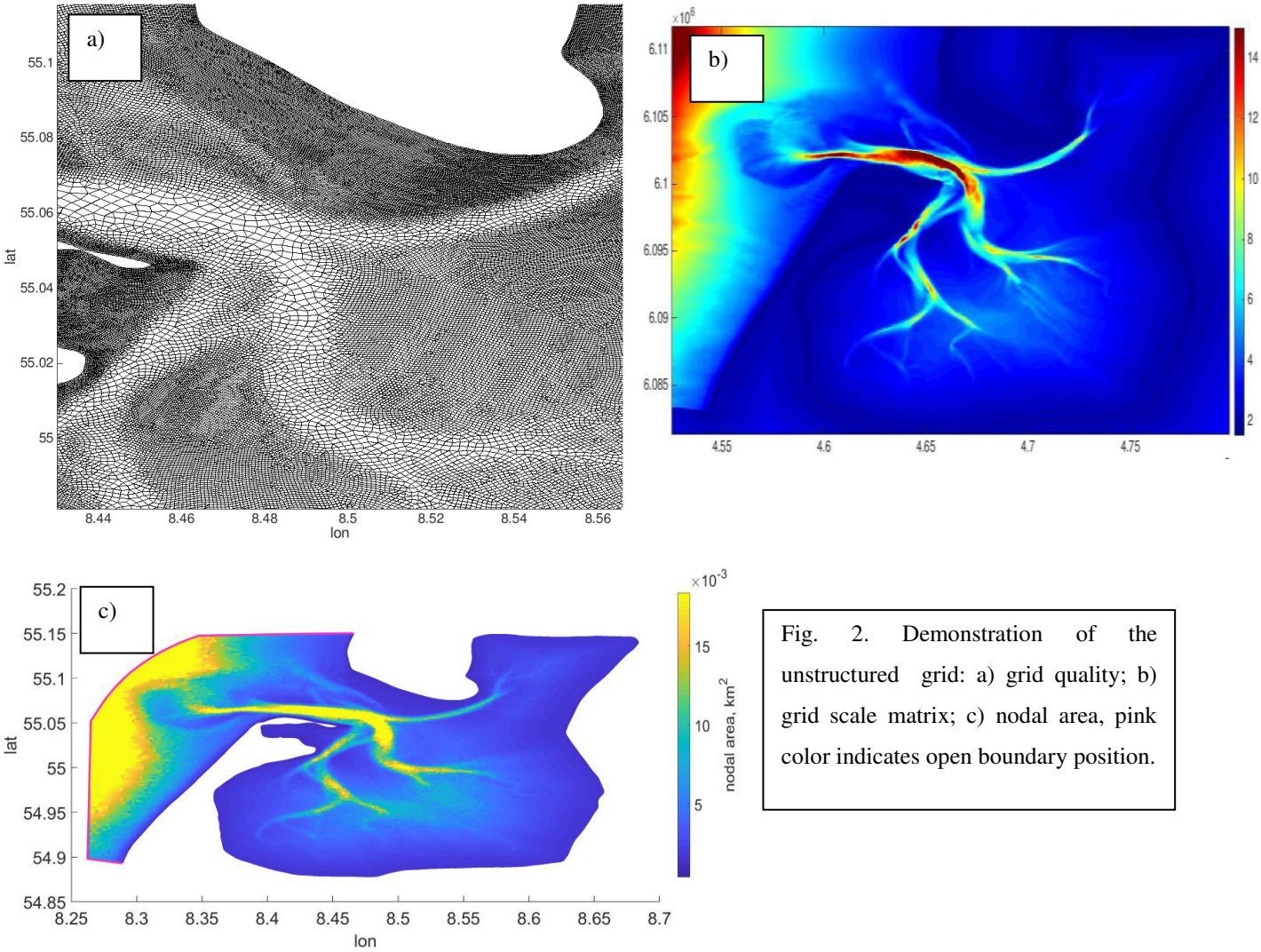

Fig. 2. Demonstration of the unstructured grid: a) grid quality; b) grid scale matrix; c) nodal area, pink color indicates open boundary position.

In case of the mixed mesh (unstructured grid) we were more flexible in choosing of the grid sizes. The matrix of element sizes was constructed based on the information about the bathymetry, the bathymetry gradient and the zones of particular interest (Lister Deep; main draining channels). Figure 2 shows the grid quality and nodal area.

Both grids have nearly the same open boundary position.

The additional figures have been added to Appendix, the additional notes have been added to the text of the manuscript.

line 103: Which turbulence closure model are you using? E.g. k-epsilon, or one of the Generic Length Scale models that GOTM provides?

The k-epsilon closure was used. The information has been added to the text.

Section 2.3: The reference to the NEMO model is inaccurate. I presume that in this study the European north-west shelf model is used and it should be cited appropriately. Why do you compute tidal harmonics from the shelf model results? This potentially introduces an error source; it would be better to use the elevation time series itself as it includes atmospheric effects. Open data: Are the bathymetric and ADCP data sets introduced in this manuscript publicly available?

Yes, the European north-west shelf model results were used, the ocean part of which is based on NEMO. We have completed the reference by citation of the web-source with full description of the setup: http://marine.copernicus.eu/services-portfolio/access-to-products/?option=com_csw&view=details&product_id=NORTHWESTSHELF_ANALYSIS_FORECAST_PHY_004_013

We did not take the elevation directly, because in this study we did not include the wind forcing. We took for the analysis the elevation time series for the whole year, therefore we hope that the analysis mistake is sufficiently small.

The ADCP data used in this study are available in PANGAEA: https://doi.pangaea.de/10.1594/PANGAEA.894070

The bathymetry data will be made publicly available this year or in the beginning of the next year and also will be available in PANGAEA database.

The additional information has been added to the text.

Section 2: The model configuration should be elaborated. What were the calibration and analysis period(s)? What were the initial conditions? Was there a spin-up period? It appears that open boundary conditions were calibrated with a 2D model using bottom drag parametrization (lines 224-226), while subsequent results were carried out with a 3D model. For clarity, please define these configurations.

All results demonstrated in the manuscript are obtained based on barotropic simulation with tidal forcing only. To find optimal tidal solution at the open boundary we performed series of 2D experiments, mainly, because the intercomparion with observations was performed based on depth-averaged velocities. After that we moved to multi-layer task. The optimal roughness height was set to 0.001 m for the TPXO9 solution; this value agreed with one estimated from observations in a similar region (Werner et al., 2003) and, in terms of the mean, with the Cd equaled to 0.0025 for the 2D-scenario (we made series of sensitivity experiments to find this value). Table 1 presents the comparison of the RMSD and Correlation coefficient with the available ADCP data for 2D and 3D cases on 1st grid with Cd=0.0025 and r=0.001 m. Table 1 shows that 2D and 3D cases show similar results in terms of intercomparison with observations.

N of obs.	**Date in May**		**TPX09, curvilinear grid, 3D case, z_0=0.001**	**TPX09, curvilinear grid, 2D case, C_d=0.0025**
655	**22**	**RMSD**	0.28	0.28
		C.C. u, v	0.87, 0.86	0.87, 0.85
637	**23**	**RMSD**	0.31	0.31
		C.C. u, v	0.82, 0.82	0.82 0.82
618	**24**	**RMSD**	0.31	0.31
		C.C. u, v	0.84, 0.7	0.84, 0.66

764	**29**	**RMSD**	0.29	0.3
		C.C. u, v	0.89, 0.89	0.89, 0.87
1259	**30**	**RMSD**	0.25	0.26
		C.C. u, v	0.97, 0.78	0.97, 0.76

The spin-up period for all simulations was three months with a criteria of the stabilization of the total energy behavior. Due to the fact that paper considers only the tidal dynamics for the analysis we took last two full tidal cycles - 59 days. We simulated the tidal dynamics in 2018, which is expressed in Doodsen correction of the prescribed amplitudes and phases, therefore we were able to compare velocities second to second.

The additional setup details have been added to the manuscript.

Harmonic analysis: The observations of velocity and water elevation observations do include atmospheric effects which are absent in the tidal models. What were the atmospheric conditions during the calibration and validation periods? Can you estimate their impact on the error metrics? Are the tides in this small-scale system really stationary so that harmonic analysis is well defined?

Table 1. Summary of the five cruises on board of Research Vessel Mya II, profiling three main transects: Inner Tidal Inlet (ITI), Main Tidal Channels (MTC) and Outer Tidal Inlet (OTI). Main Tidal Channels (MTC) show the initial, turning and ending points, since it covers three sections in one transect. The Wind Roses characterize the wind conditions during cruise times, with the legend colors representing the wind velocity in m/s and the circles representing the frequency percentage of the direction from where the wind blows.

Transect Name	Date	Lon / Lat (°) (Start – End)	Tidal Period	Duration (h)	Wind conditions (Wind Rose)

ITI	22/05/2018	8.464 55.047 8.489 55.062	/ / 	neap	6:28	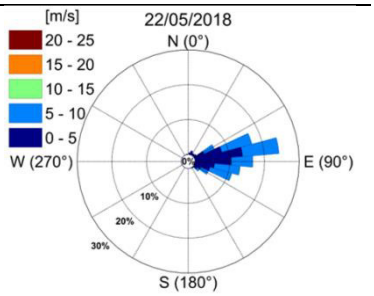
MTC	23/05/2018	8.461 55.039 8.474 55.035 8.499 55.046	/ / / 	neap+1 day	6:19	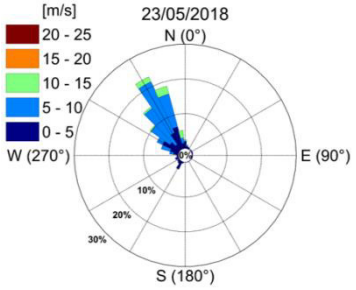
	24/05/2018	8.505 55.056	/	neap+2 days	5:56	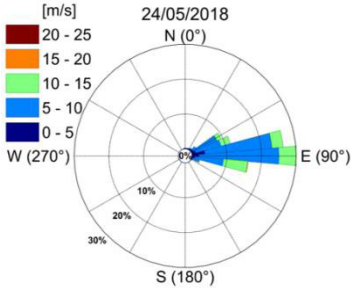
ITI	29/05/2018	8.464 55.047 8.489 55.062	/ / 	spring	7:11	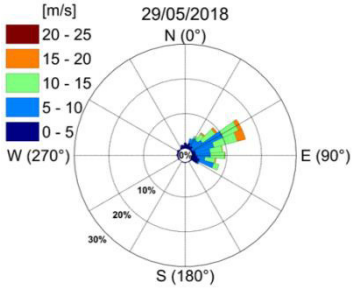
OTI	30/05/2018	8.418 55.059 8.428 55.071	/ / 	spring+1 day	12:24	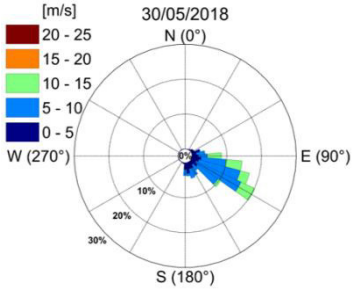

The main wind direction during the cruises was around the 90° (East) sextant, with the most frequent intensities in the range of 5 to 10 m/s. During 24th of May the wind was blowing strongly from the east nearly during the whole cruise. Exceptions were the cruise on May 23 concerning the direction, when were observed winds from the NNW (330°), and the cruise on May 29 with mostly frequent intensity ranging between 10 to 15 m/s.

Table 2 in the manuscript shows that for all solutions except FES, the correlation coefficients are higher during spring tides as well as in the deepest part of the domain despite the quite strong winds often ranging from 10 to 15 m/s 29th and 30th of May. The largest velocity errors for all solutions occur when tidal velocities are small as well as during the tidal state change, so we can guess that at these moments wind, wave and baroclinicity effect become much more pronounced. On May 23 and May 24, the measurements were performed on nearly the same side; but the May 24 correlation coefficient for the 'v' component is relatively small. In this case we can really say that the reason is permanent wind from the east. However in this zone, tides seem to be explained more than 80 % (or 90 % or more in case of a spring tide) of the dynamics in case of absent storm (more than 20 m/s) and blowing continuously in one direction winds.

We believe that the wind forcing will add approximately the same contribution to error for all boundary conditions used based on very high correlation coefficients.

The FFT analysis of the modeling results was done after the stabilization of the total energy behavior. The elevation signal from TG was analyzed based on the whole year time-series. Due to the fact that the frequencies induced by wind are very high, we believe that this is high quality analysis. However, of course, some errors are there, which are hard to correct.

The 'wind' table has been added to the Appendix.

line 195: Is Cd constant in space? If so, is that a realistic configuration for the bight?

Tide gauge comparisons: It would be useful to have example time series comparing the observations and the model to give a better idea of the model's performance. A

Taylor diagram could also be used.

Yes, we took Cd as a constant for the region due to the fact that the seabed habitat map is not ready yet for the area, there are nearly no observations in the shallow part of the region and considered area is relatively small. Therefore we think that such a decision is justified.

The reconstructed tidal elevation from observations based on FFT and elevation based on model runs visually are nearly identical. The intercomparison example of the observed and modeled amplitudes at the gauging station + Taylor diagrams for amplitude and phase are given below. The diagrams were added to supplementary materials.

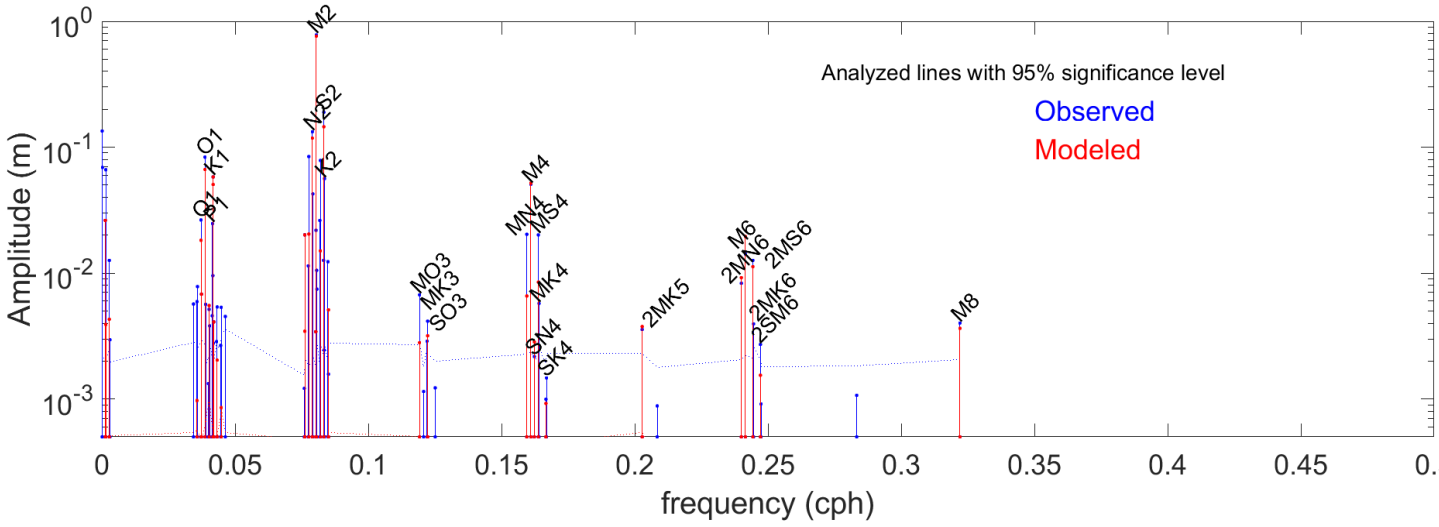

Fig. Demonstration of the FFT analysis results at List TG.

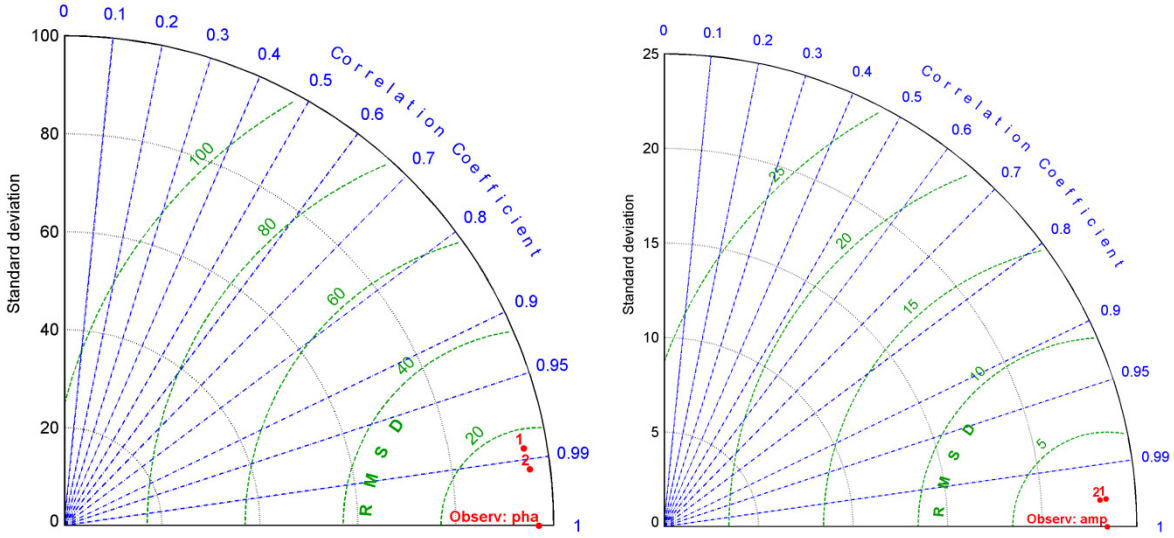

Taylor diagrams based on observed and modelled data at 3 gauging stations, '1' and '2' indicate simulation results on curvilinear and unstructured grids respectively: a) for amplitude; b) for phase.

line 219: Do you use a sponge layer? If so, please describe it in Section 2.
Thank you for the comment.

To avoid errors due to the inconsistency between the character of equations and the specified open boundary conditions (prescription of tidal elevation only), a 3-km sponge layer has been introduced. It gradually turns off the advection of momentum and viscosity in the vicinity of the open boundary (Androsov et al., 1995). The appropriate information is added to the manuscript.

Androsov, A.A., Klevanny, K.A., Salusti, E.S., Voltzinger, N.E.: Open boundary conditions for horizontal 2-D curvilinear-grid long-wave dynamics of a strait, Advances in Water Resources, 18, 267–276, 10.1016/0309-1708(95)00017-D, 1995.

Baroclinicity: The tidal dynamics, e.g. tidal ellipses, are probably affected by density and stratification effects which in the present study is neglected. Can you argue that baroclinic effects are negligible in this system?

The water column in the domain of interests is generally well mixed, weak strain induced periodic stratification only occurs at the end of the flood in some subareas (Villarreal et al., 2005; Simpson et al., 1990; Purkiani et al., 2015). So we think that for the **depth-averaged** ellipse maps we can omit baroclinic effect. The presence of the weak density gradient in the system has an influence to the local

circulation, especially in the Lister deep zone. But there the tidal residual circulation is large and would dominant the dynamics. We think that our results are valid in case of baroclinic effects are turned on, however further consideration of the SPM budget would be not possible without considering baroclinicity (e.g., Burchard et al., 2008).

Burchard, H., Flöser, G., Staneva, J. V., Riethmüller, R. and Badewien, T.: Impact of density gradients on net sediment transport into the Wadden Sea, J. Phys. Oceanogr., 38, 566 – 587, https://doi.org/10.1175/2007JPO3796.1, 2008.
Purkiani, K., Becherer, J., Flöser, G., Gräwe, U., Mohrholz, V., Schuttelaars, H. M. and Burchard, H.: Numerical analysis of stratification and destratification processes in a tidally energetic inlet with an ebb tidal delta, J. Geophys. Res-Oceans, 120, 225– 243, https://doi.org/10.1002/2014JC010325, 2015.
Simpson, J.H., Brown, J., Matthews, J. et al. Estuaries (1990) 13: 125. https://doi.org/10.2307/1351581.
Villarreal, M.R., K. Bolding, Burchard, H., and E. Demirov, 2005. Coupling of the GOTM turbulence module to some three-dimensional ocean models, Marine Turbulence: Theories, Observations and Models, Baumert, H. Z., J. H. Simpson, and J. Sündermann, Eds., Cam-bridge University Press, Cambridge, 225–237.

Section 5.2: Larger dissipation in the unstructured grid could also be due to better resolved intertidal dynamics that are inherently dissipative. Presumably also the bathymetric features are quite different in these two grids.

Thank you for the comments. We agree that better resolved intertidal dynamics can be an additional factor of the larger dissipation. This part of the dissipation can be largely traced in the behavior of the bottom friction and energy change adds of the balance. The conclusion about larger dissipation on the unstructured grid is made based on analysis of the energy imbalance. We should stress that the unstructured grid is more dissipative numerically anyway with our type of discretization, this is well proofed result (e.g. Danilov and Androsov, 2015; Androsov et al., 2019).

The additional comments have been added to the text.

Danilov, S. and Androsov, A.: Cell-vertex discretization of shallow water equations on mixed unstructured meshes, Ocean Dynam., 65, 33 – 47, https://doi.org/10.1007/s10236-014-0790-x, 2015.
Androsov, A., Fofonova, V., Kuznetsov, I., Danilov, S., Rakowsky, N., Harig, S., Brix, H., and Wiltshire, K. H.: FESOM-C v.2: coastal dynamics on hybrid unstructured meshes, Geosci. Model Dev., 12, 1009 – 1028, https://doi.org/10.5194/gmd-12-1009-2019.

The authors conclude that the model results "converge" to a realistic solution (line 81,

478, abstract), based on the presented simulations with two different grids. The authors also conclude that the curvilinear grid has lower dissipation making it thus better suited for baroclinic studies. I find these conclusions somewhat premature: Only two different grids were used, which at the same time had different element types (triangles and quads), resolution and topology (unstructured and curvilinear), as well as (I presume) bathymetry. As such, it is really quite hard to infer what grid properties cause the observed change in model performance. The grid sensitivity study should be extended to better address the effects.

We made a study of convergence of the solution on meshes of different configurations (quadrilateral, triangular and mixed) for the studied region in the work of Androsov et al., 2019. The study is based on coarser meshes and bathymetry data and with only M2 forcing. However, it provides a comparative analysis of energy characteristics as well as a histogram of errors of dynamical characteristics on meshes of different configurations. As was mentioned above it is proofed fact that the quadrilateral (curvilinear) has lower numerical dissipation with our desritization. We agree that this a premature to talk about which grid will better in case of baroclinic study, it is actually should be checked in further work. We have decided to write additional small article dedicated to the reproduction of the nonlinear effects on the grids of different structure. The bathymetry matrix was the same for both grids. We have added the reference to the manuscript and additional notes.

Androsov, A., Fofonova, V., Kuznetsov, I., Danilov, S., Rakowsky, N., Harig, S., Brix, H., and Wiltshire, K. H.: FESOM-C v.2: coastal dynamics on hybrid unstructured meshes, Geosci. Model Dev., 12, 1009 – 1028, https://doi.org/10.5194/gmd-12-1009-2019.

Technical corrections

line 123: 1/30 *degree*

line 182: this paragraph is duplicate of the previous one.

Figure 3 a: The ratio being thus defined it would be more appropriate to call it "weight of linearity" instead. The unit (m) is wrong.

Table 3: Add units. What do "RMSD", "amp(cm)", "ph(_)" stand for?

Figure 9: Add units.

Thank you a lot! Done.

Referee 2

The article is a detailed study of the nonlinear dynamics of the tide in the shallow bay of the North Sea, which is characterized by a significant area of the intertidal zone. As a research tool, a relatively new FESOM-c model is used, which approximates the governing equations by the finite volume method and is able to work on hybrid unstructured computational grids. New data on the bathymetry of the bay and tidal currents are also presented. The authors of the study set a rather difficult goal, analyzing the results of observations and modeling for the summary tide instead of effects of nonlinearity for the single harmonic tide. In the latter case, it would be easier to estimate the contribution of the main mechanisms of nonlinearity (shallow depth, advection, and quadratic friction) on the structure of tidal asymmetries. Nevertheless, the results presented in the article are of real interest, since they provide a serious basis for analyzing the features of sediment dynamics and the formation of a variable bottom relief. I would recommend this paper to be published after a little revision. I hope the comments below help improve the manuscript.

Dear Referee 2,

Thank you so much for the very valuable comments! Please, find the answers below. We agree, that further study should be dedicated to the analysis of the separate mechanisms of nonlinearity in the domain based on grids with different structure.

Kind regards, Vera on behalf of the co-authors

Specific comments:

Line 100: Are only 10 sigma vertical layers enough for 3D simulations? In other words, is the numerical solution dependent on the number of vertical layers?

Thank you for the question. The water column in the domain of interests is generally well mixed, weak strain induced periodic stratification only occurs at the end of the flood in some subareas (Villarreal et

al., 2005; Simpson et al., 1990; Purkiani et al., 2015). Based on available observations we can conclude that the vertical structure of the velocities and turbulent characteristics are relatively simple (Burchard et al., 2008, Purkiani et al., 2015)

As soon as we have concentrated our attention mainly on the depth-averaged dynamics and near-bottom dynamics (our vertical layers are crowded near the bottom) and the area of consideration is relatively shallow, we have agreed on 10 levels.

Burchard, H., Flöser, G., Staneva, J. V., Riethmüller, R. and Badewien, T.: Impact of density gradients on net sediment transport into the Wadden Sea, J. Phys. Oceanogr., 38, 566 – 587, https://doi.org/10.1175/2007JPO3796.1, 2008.
Purkiani, K., Becherer, J., Flöser, G., Gräwe, U., Mohrholz, V., Schuttelaars, H. M. and Burchard, H.: Numerical analysis of stratification and destratification processes in a tidally energetic inlet with an ebb tidal delta, J. Geophys. Res-Oceans, 120, 225– 243, https://doi.org/10.1002/2014JC010325, 2015.
Simpson, J.H., Brown, J., Matthews, J. et al. Estuaries (1990) 13: 125. https://doi.org/10.2307/1351581.
Villarreal, *M.R.*, *K. Bolding*, *Burchard*, *H.*, and *E. Demirov*, 2005. *Coupling* of the *GOTM turbulence module* to *some three-dimensional ocean models*, Marine Turbulence: Theories, Observations and Models, Baumert, H. Z., J. H. Simpson, and J. Sündermann, Eds., Cam-bridge University Press, Cambridge, 225–237.

Section 2.3 (Open boundary conditions) Please specify the period of model calculations (dates).

The spin-up period for all simulations was three months with a criteria of the stabilization of the energy behavior. Due to the fact that paper considers only the tidal dynamics for the analysis we took last two full tidal periods - 59 days. We simulated the tidal dynamics in 2018, which is expressed in Doodsen correction of the prescribed amplitudes and phases, therefore we were able to compare observed and modeled velocities second to second for end of May 2018.

The additional setup details have been added to the manuscript.

Line 165 (Data. 3.2 Tide gauge (TG) data): VidaTG station is located in the intertidal zone, and so during low tide (when the seabed is exposed) the continuous (quasi harmonic) time series is greatly distorted. (see for example, https://www.emodnetphysics.eu/map/platinfo/piroosplot.aspx?platformid=9015&60days=true). In fact, this is time series with data gaps. Nevertheless, the authors used classical harmonic analysis for this station in the validation of the model. Did authors take into account the

peculiarity of the tide in this station when analyzing the results? (see also the comment below on Section 4.5.2).

Thank you for the question. VidaTG station is situated in the intertidal zone, however itself is situated in the quite deep channel, therefore there is no distortion of the time series (Fig. 1).

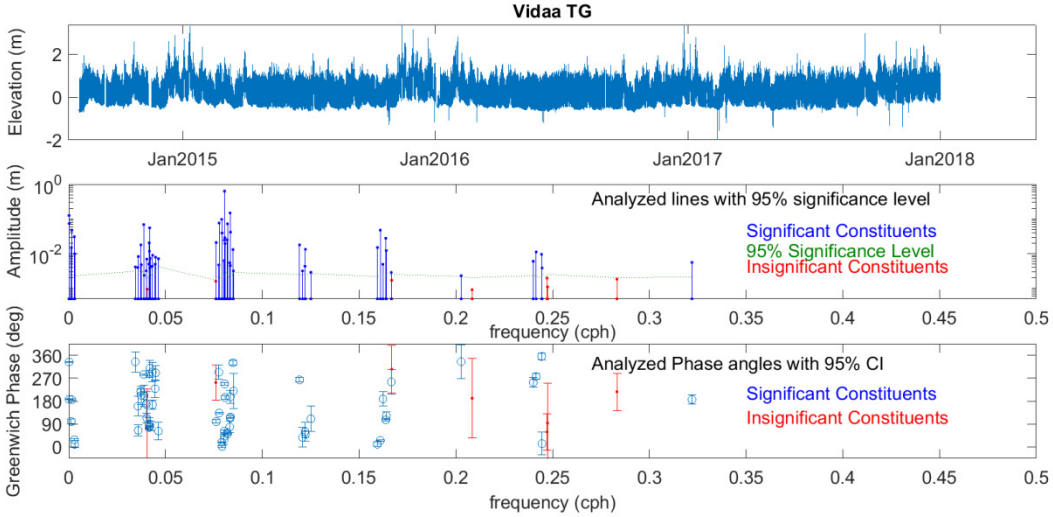

Figure 1. The elevation time series at the Vidaa TG and results of the classical harmonic analysis.

Table 2. The results of the inter comparison show rather large RMSD values (compared with the velocity values themselves). Apparently, this is due to the neglect of wind induced fluctuations in the simulation. The question arises: Is inter comparison in Table_2 appropriate?

Thank you for the question. We think that the wind forcing will add approximately the same contribution to the error for all boundary conditions used based on very high correlation coefficients. In considered zone tides seem to be explained more than 80 % (or 90 % or more in case of a spring tide) of the dynamics in case of absent storm (more than 20 m/s) and blowing continuously in one direction winds. On this basis, we give this comparison in Table 2, the purpose of which is to select those boundary conditions that have the smallest absolute error compared to the observational data.

Line 330: It seems to me that the use of the term “seiche” is not entirely appropriate in

this context, since we are dealing with forced fluctuations. It would be more correct to speak about oscillations as near standing wave.

We replaced the term “seiche” with a more general term – “standing wave”.

Line 350: It is desirable to immediately emphasize that the results of Fig. 8 relate to the sea level (not currents).

Thank you for the comments. We have put additional notes to the figure caption.

Line 359: Frankly, I do not see indication on degenerate amphidromic point in external area. Yes, there is a slight closeness of phase contours lines (caused by proximity to the strait and refraction of the tidal wave), but there is no decrease in the tide amplitude as it is usually in nodal (amphidromic) zone. The effect of the capture of a Poincare wave is interesting, but requires explanation or reference.

Thank you. Absolutely correct remark, this picture does not clearly show the presence of amphidromic point, because we do not see a concentric decrease in the level. We have excluded this conclusion from the text.

Line 365-370: It is interesting how the authors distinguish between the different duration of the ebb and tide caused by the nonlinearity from the effect of the sum of harmonics of various periods. The last effect is called the Diurnal Inequality of tide, and it is not connected with non-linearity.

Thank you very much for the very useful remarks! The features represented in Fig. 9 (level panel) show the mean pattern for the full tidal cycle (29.5 days). However, we should definitely pointed out that the reason of the variations in Fig. 9 (right panel) is not only non-linear effects, but also Diurnal Inequality of tide. The additional comments have been added to the text.

Line 405-410: To explain the effect of the dominance of tide velocities over ebb ones, it is not necessary to use phase speed inequality (SQRT (gh)). There is a simple explanation for this effect: the bottom friction dampens the flow more efficiently in smaller depth (during low ebb).

We agree to the comments. However, in this zone, the depth is relatively large and residual circulation is smallest compared to the surrounding area.

The mentioned effect induced by bottom friction can be traced in the zone 2, where we have an extensive intertidal zone and maximum amplitudes of the semidiurnal tides compared to other zones, here the flood dominance can be explained by the major role of non-linear friction effects and non-linearity in changes of the water-layer thickness.

Section 4.5.2 (Line 412). Again about the accuracy of harmonic analysis in the intertidal zone. Indeed, in this zone, at low tide, the bottom is exposed, and this means that data gaps appear in the model time series. In this case, the classical harmonic analysis can give inaccurate results for the amplitudes and phases of the waves. It seems that it would be more logical to exclude intertidal zones from the analysis of results (at least in terms of the results of harmonic analysis). How was this fact taken into account? Otherwise it's necessary apply special procedures to avoid mistakes.

Thank you a lot for the comment. We agree with the remark. We have decided to consider intertidal zone, because it occupies at about 40 % of the whole considered area. We performed our simulations with time step of about 1 s, we did not do any averaging and used output every couple of seconds to perform the analysis. Therefore, analyzing last two full tidal cycles (29.5 × 2 days), we had large time-series. Also we have performed sensitivity test (modifying the analyzed period), which showed that the results of the analysis are justified.

Section 6 (Summary). Unfortunately, the question of the sensitivity of the numerical simulation to the accuracy of bathymetric data remained outside the discussion. In particular, how important is the effect of new bathymetric data in the strait on simulation results. A comparison of the solutions with the old and new bathymetry would answer this question, and perhaps provide a serious justification for the need for new good bathymetry for the whole area.

Important note. Thanks. At a preliminary stage, comparison analysis of results of the computation for three bathymetric databases is carried out: 200 m (H. Burchard, personal communication), 100 m and with a resolution of 50 m (L. Sander, personal communication). The meshes used in this analysis have a rectangular structure and the spatial resolution corresponding to the bathymetry info. Note, that 200 m bathymetry is largely smoothed compared to 50 m bathymetry product. Results were analyzed on fields of residual circulation in a tidal cycle of M2 wave. The residual circulation based on high quality bathymetry data considerably differs from one based on a coarser bathymetry (figures below). Vortex structures have some space shift, a considerable intensification on detailed bathymetry in comparison with smoothed one (figures below).

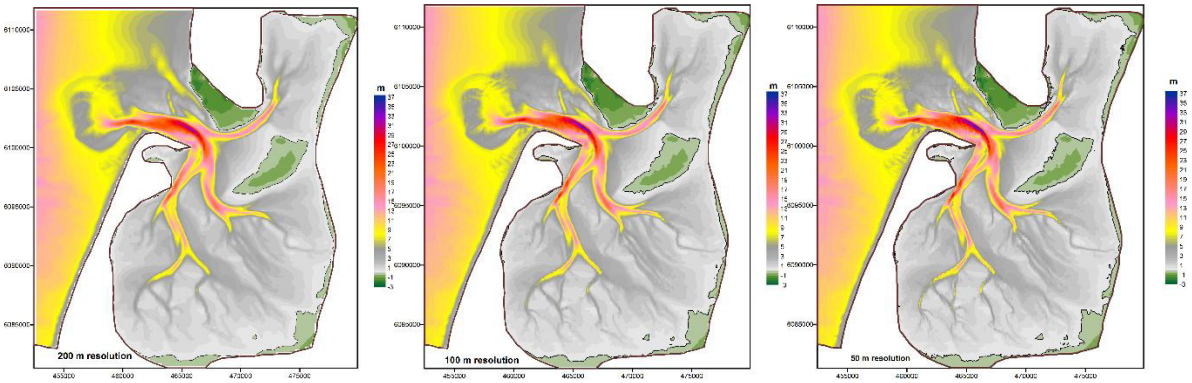

Bathymetry. Left – 200 m resolution; middle – 100 m; right – 50 m.

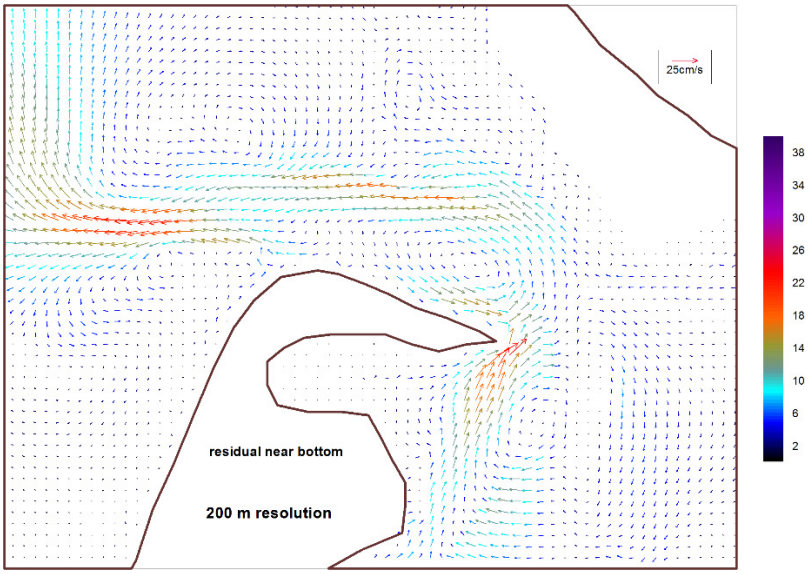
25cm/s
38
34
30
26
22
18
14
10
6
2
residual near bottom
200 m resolution

380

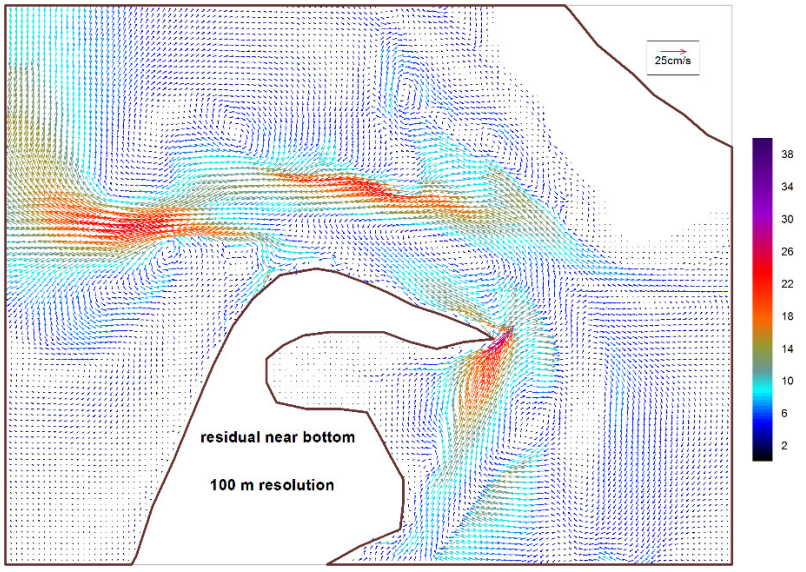
25cm/s
38
34
30
26
22
18
14
10
6
2
residual near bottom
100 m resolution

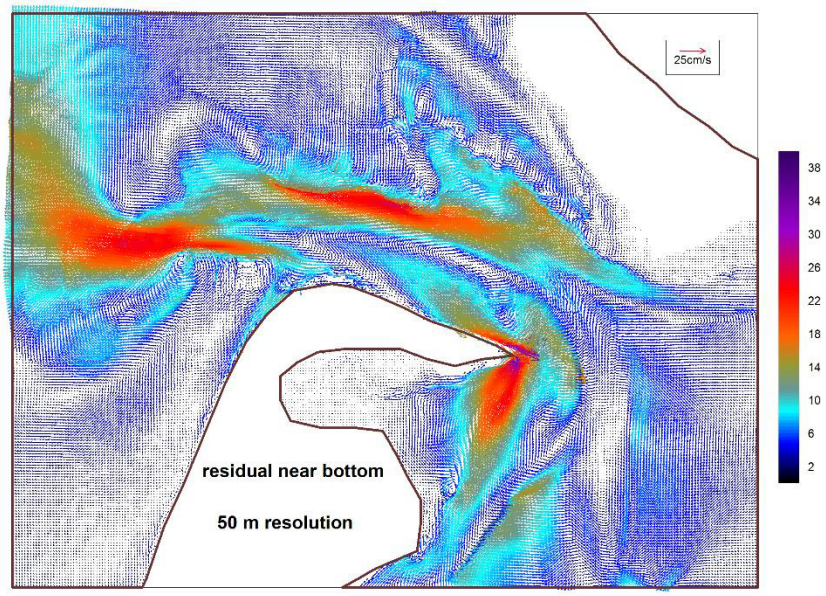

Residual circulation near bottom. M2 wave. Upper panel – 200 m bathymetry resolution; middle panel – 100 m resolution; bottom panel – 50 m.

Technical corrections:

Lines 175 and 182: Two paragraphs contain the same information.
Line 245: 29.5 days is rather a lunar (synodic) month than a tidal cycle
Line 335: Direction of rotation (not orientation) of the tidal ellipse is determined by the sign of the ellipticity. (Orientation is rather the inclination of its main axis of the ellipse).
Line 372: Replace “(level panel)” by “(left panel)”
Figure 5. Please explain what the following sentence means: "The length of vectors on the maps is scaled based on the square root method."
Figure 8 .: “The dark blue color indicates zone, where topography features are above sea level.” ..... above the highest sea level ???

Thank you a lot! Done

Referee 3

Dear Referee 3,

Thank you for the comments. Please, find the answers below.

Kind regards, Vera on behalf of the co-authors

This is a high resolution hydrodynamic modelling study of a region of the Wadden Sea. A new bathymetric product for the region has been incorporated as model input, allowing for higher resolution simulations to be conducted – but what are the implications of this to the wider field? Overall, I felt that although the methods were sound, the paper lacked novelty and read as more of a 'site characterisation' study than a piece of novel research. My main comment is that the authors could do more to convince the readers that this is an interesting region to study, and to describe more clearly what this paper adds to the field of knowledge on the area/ implications for future modelling studies. Further still, there are numerous ambiguous and subjective statements made. Because of the lack of explicit motivation for the importance/relevance of this work, I found the lengthy results section difficult to follow. On this basis, I would recommend that the manuscript be returned to the authors for a major (editorial) revision, to include the re-working of many of the figures. My apologies that it has taken me a long time to return this review.

Importance/relevance

The tidal residual circulation and asymmetric tidal cycles largely define the transport and accumulation of sediment and the distribution of bedforms in the bight. Largely due to gap in understanding of the asymmetric tidal cycles phenomena, in the literature you can find different values of suspended matter fluxes and the sediment budget in/of the bight (e.g., Boldreel et al., 2010; Burchard et al., 2008; Hayes, 1980; Nortier, 2004; Postma, 1967). Even the estimate of the relatively simple value as the mean water volume entering the basin during flood and leaving during ebb in a mean sense varies from 4 to 6.3 $*10^8$ m^3 (Bolaños-Sanchez et al., 2005; Gätje and Reise, 1998; Gräwe et al. 2016; Lumborg and Windelin, 2003; Nortier, 2004; Pejrup et al., 1997; Purkiani et al. 2015).

Novelty, major points

scientific

- Four zones with fundamentally different asymmetry structures were indicated during tidal asymmetry analysis.
- Tidal asymmetry maps were firstly introduced and constructed.
- Tidal ellipses, energy fluxes and residual circulation maps were constructed and analyzed.

Based on this analysis you can largely judge about the velocity behavior, water parcel trajectories and bedform peculiarities in the area.

methodical

- For the first time the bathymetry product with such a high resolution was used for the area.
- The two new grids with different structure were constructed and convergence of the results were shown.
- The best tidal solution at the open boundary for the area was identified.

Comment to the hand-written remark:

- Spaces must be included between number and unit (e.g. 1 %, 1 m) according to the journal rules.
- Please, consider that the quality of the pictures in the manuscript is not the best to reduce the size of the pdf.
- The manuscript was proofread by the native speaker except the Discussion Section.

Bolaños-Sanchez, R., Riethmüller, R., Gayer, G. and Amos C. L.: Sediment transport in a tidal lagoon subject to varying winds evaluated with a coupled current-wave model, J. Coastal Res., 21, e11 – e26, https://doi.org/10.2112/03-0048.1, 2005.

Boldreel, L. O., Kuijpers, A., Madsen, E. B., Hass, H. C., Lindhorst, S., Rasmussen, R., Nielsen, M.G, Bartholdy, J. and Pedersen, J. B. T.: Postglacial sedimentary regime around northern Sylt, South-eastern North Sea, based on shallow seismic profiles. Bull. Geol. Soc. Den., 58, 15 – 27, 2010.

Burchard, H., Flöser, G., Staneva, J. V., Riethmüller, R. and Badewien, T.: Impact of density gradients on net sediment transport into the Wadden Sea, J. Phys. Oceanogr., 38, 566 – 587, https://doi.org/10.1175/2007JPO3796.1, 2008.

Gätje, C. and Reise, K. (Eds.): Ökosystem Wattenmeer: Austausch-, Transport- und Stoffumwandlungsprozesse, Springer, Berlin, Heidelberg, Germany, https://doi.org/10.1007/978-3-642-58751-1, 1998.

Hayes, M. O.: General morphology and sediment patterns in tidal inlets, Sediment. Geol., 26, 139 – 156, https://doi.org/10.1016/0037-0738(80)90009-3, 1980.

Gräwe, U., Flöser, G., Gerkema, T., Duran-Matute, M., Badewien, T. H., Schulz, E. and Burchard, H.: A numerical model for the entire Wadden Sea: Skill assessment and analysis of hydrodynamics, J. Geophys. Res-Oceans, 121, 5231 – 5251, https://doi.org/10.1002/2016JC011655, 2016.

Nortier, R. J.; Morphodynamics of the Lister Tief tidal basin. M. S. thesis, TU Delft, Netherlands, pp. 76, available at: http://resolver.tudelft.nl/uuid:89da7250-9acb-429d-bb71-d7dbc60e7755, 2004.

Pejrup, M., Larsen, M. and Edelvang, K.: A fine-grained sediment budget for the Sylt-Rømø tidal basin, Helgolander Meeresun., 51, 253 – 268, https://doi.org/10.1007/BF02908714, 1997.

Postma, H.: Sediment transport and sedimentation in the estuarine environment, in: Estuaries, edited by: Lauff, G. H., American Association for the Advancement of Science, Washington, DC, 158 – 179, 1967.

Purkiani, K., Becherer, J., Flöser, G., Gräwe, U., Mohrholz, V., Schuttelaars, H. M. and Burchard, H.: Numerical analysis of stratification and destratification processes in a tidally energetic inlet with an ebb tidal delta, J. Geophys. Res-Oceans, 120, 225– 243, https://doi.org/10.1002/2014JC010325, 2015.

Lumborg, U. and Windelin, A.: Hydrography and cohesive sediment modelling: Application to the Rømø Dyb tidal area, J. Marine Syst., 38, 287 – 303, https://doi.org/10.1016/S0924-7963(02)00247-6, 2003.

I have included some general comments below. I have made many hand-written notes on the manuscript that should point to where I saw the above issues manifested (please see the attached scanned document). I stopped correcting the language on page 8, but ambiguous terms remain which need to be edited out. What are “patchy dynamics”? What are velocities which are “nearly always larger”? Please quantify, expand, elaborate, justify and support your statements.

Thank you for the comments. We have included the corrections to the manuscript based on your notes.

General comments

1. The abstract could do with opening with a broader, overarching introduction of the topic, rather than launching into what is done here.

The abstract was modified.

2. The language used was subjective in places (e.g. “ the quite good results”) – please take care to make all statements objective.

We made the corrections. We left some 'subjective' sentences, where we have directly link to the numbers (such as a reference to the tables).

3. Can you avoid referring to the grids as first and second grids (which is confusing), but instead refer to them as ‘curvilinear’ and ‘unstructured’ (or similar, as appropriate).

Done

4. line 194 – what were these additional experiments? It’s fine not to show them, but what were they and how did you get to the conclusion that you draw?

Thank you for the comment, now we can add a reference, where these experiments are described. It has been done.

5. Line 200 – same or worse results? Please elaborate.

Here, the major point that we were not able to improve the correlation coefficient and RMSD varying further bottom friction coefficient. The changes in the text have been done.

6. Line 224-225, please can we have a range of depth layer thicknesses and explain how these were parameterized, e.g. terrain-following?

The 10-sigma (terrain-following) vertical layers were prescribed. The distribution of the sigma layers satisfies the parabolic function. The minimum possible thickness of the vertical layer is ~1 cm.

sigma(k)=-[(k-1)/(kb-1)]^2, kb is a total amount of sigma layers, k is current layer (k=1..kb), sigma=-1 at the bottom, sigma=0 at the surface.

7. Line 237 – " the same probably holds". This is ambiguous, and does not fill me with confidence in the rest of your interpretations, please can you clarify, and back this statement up?

We agree that this statement, probably, needs a detailed interpretation, so we have decided to remove it.

8. Please revise the figure colour scales! Please improve upon the multi-coloured ones, as a matter of priority. Figures 3, 6, 8 and 9, in particular, are impossible to interpret. 9. Figure 4, pink and red difficult to differentiate, please consider dashed lines or something, so that these are meaningful even in black and white. 10. The vector plots cannot be interpreted, these need to be made clearer. Fewer arrows perhaps? Please reconsider how these data are presented.

We changed the figures based on your comments and hand-written notes.

11. The discussion is short and lacking depth and detail. What have you found, what are the implications, and for whom? Please revise and improve.

The discussion of the manuscript was modified.

Non-linear aspects of the tidal dynamics in the Sylt-Rømø Bight, south-eastern North Sea

Vera Fofonova[1,2], Alexey Androsov[1,3], Lasse Sander[2], Ivan Kuznetsov[1], Felipe Amorim[2], H. Christian Hass[2], Karen H. Wiltshire[2]

[1] Alfred Wegener Institute, Helmholtz Centre for Polar and Marine Research, Bremerhaven, 27570, Germany
[2] Alfred Wegener Institute, Helmholtz Centre for Polar and Marine Research, List/Sylt, 25992, Germany
[3] Shirshov Institute of Oceanology, Moscow, 117997, Russia

Correspondence to: Vera Fofonova (vera.fofonova@awi.de)

Abstract. This study is dedicated to the tidal dynamics in the Sylt-Rømø bight with a focus on the non-linear processes. The FESOM-C model was used as the numerical tool, which works with triangular, rectangular or mixed grids and is equipped with a wetting/drying option. As the model's success at resolving currents largely depends on the quality of the bathymetric data, we have created a new bathymetric map for an area based on recent studies of Lister Deep, Lister Ley, and the Højer and Rømø Deep areas. This new bathymetric product made it feasible to work with high resolution grids (up to 2 m in the wetting/drying zone). As a result, we were able to study the tidal energy transformation and the role of higher harmonics in the domain in detail. For the first time, the tidal ellipses, maximum tidally-induced velocities, energy fluxes and residual circulation maps were constructed and analysed for the entire bight. Additionally, tidal asymmetry maps were introduced and constructed. The full analysis was performed on two grids with different structures and showed a convergence of the results as well as fulfillment of the energy balance. A great deal of attention has been paid to the selection of open boundary conditions, model validation against tide gauges, and recent in-situ current data. The tidal residual circulation and asymmetric tidal cycles largely define the circulation pattern, transport and accumulation of sediment and the distribution of bedforms in the bight, therefore the results presented in the article are necessary and useful benchmarks for further studies in the area, including baroclinic and sediment dynamics investigations.

1 Introduction

The Sylt-Rømø Bight (SRB) is one of the largest tidal catchments in the Wadden Sea, which stretches from the Dutch island of Texel to Skallingen, a peninsula in Denmark. The SRB is characterized by the barrier islands Sylt (Germany) and Rømø (Denmark), which are separated by a tidal inlet called Lister Deep. Two artificial causeways, the Hindenburg Damm (1927) and the Rømøvej (1948), connect the islands Sylt and Rømø to the mainland and create a semi-enclosed back barrier environment. Water exchange with the North Sea takes place through the 2.8 km-wide Lister Deep. The main channels draining the tidal back barrier environment are called Lister Ley, Højer Deep and Rømø Deep (Fig. 1).

The bight is characterized by large intertidal areas occupying about 40 % of the entire bight. The domain of interest has an average water depth of ~4 m and a maximum water depth of ~37 m in Lister Deep (Fig. 1). The tidal range in the area is ~1.8 m (e.g., Pejrup et al., 1997) and the water column is generally well mixed (e.g., Villarreal et al., 2005). The annual mean freshwater discharge into the bay is only ~7 m^3/s (e.g., Purkiani et al., 2015).

The tides play a major role in the local bight dynamics. Estimates of maximum horizontal tidal velocities in Lister Deep vary from 1.2 to 2 m/s. Estimates of the mean water volume entering the basin during flood and leaving during ebb (the tidal prism) vary from 4 to 6.3 $\times$ 10^8 m^3 (Bolaños-Sanchez et al., 2005; Gätje and Reise, 1998; Gräwe et al. 2016; Lumborg and Windelin, 2003; Nortier, 2004; Pejrup et al., 1997; Purkiani et al. 2015). The residual circulation of the M2 wave, the dominant tidal constituent in the area, is presented in Burchard et al. (2008) and Ruiz-Villarreal et al. (2005) (wherein the grid resolution is 200 m); it shows maximum values up to 0.3 m/s in the area of Lister Deep, Lister Ley and Højer Deep edges (the zones of large bathymetric gradients). There are two large vortex structures located at the entrance of the Königshafen embayment and directly north of the island of Sylt in the western Lister Deep (Fig. 1). They have clockwise and anticlockwise directions of rotation, respectively.

There is a pronounced asymmetry in the tidal water level and current velocities behaviour, caused by complex morphological features and by the general shallowness of the area (e.g., Austen 1994; Becherer et al., 2011; Lumborg and Windelin, 2003; Nortier, 2004; Ruiz-Villarreal et al., 2005). It is known that the Lister Deep can be characterized as an ebb-dominated area, i.e. the velocities during ebb are larger compared to flood velocities in the mean and maximum senses (e.g., Hayes, 1980; Oost et al., 2017; Fig. 1). The analysis of bedforms based on seismic profiles revealed that the area around Lister Deep is represented by a complex spatial pattern of the flood- and ebb-dominated subaqueous dunes (Boldreel et al., 2010).

The tidal residual circulation and asymmetric tidal cycles largely define the transport and accumulation of sediment and the distribution of bedforms in the bight (e.g., Boldreel et al., 2010; Burchard et al., 2008; Hayes, 1980; Nortier, 2004; Postma, 1967). Note that the tide entering the Wadden Sea leaves ~3.5 $\times$ 10^6 t yr^{-1} of suspended matter there according to Postma (1981). The most intensively studied dynamic is in the area of Lister Deep (a 'bottleneck' area); it is studied more than the other subareas as it can shed light on the sediment as well as water and salt budgets of the whole bight (e.g., Kappenberg et al., 1996; Nortier, 2004; Bolaños-Sanchez et al., 2005; Becherer 2011; Purkiani et al. 2016; Gräwe et al. 2016; Lumborg and Windelin, 2003; Lumborg and Pejrup, 2005; Burchard et al., 2008; Purkiani et al., 2015; Villarreal et al., 2005). However, the listed studies offer quite different estimates of suspended matter fluxes and the sediment budget. In our opinion, one of the reasons for such disagreement is a gap in understanding of the role of the tide. In a back-barrier environment like this, higher tidal harmonics take on a relatively large role in the dynamics. For example, Stanev et al. (2015) demonstrated that a higher harmonic (M4) in the German Bight causes strong tidal asymmetry. Though continuous observational data can give answers about tidal water level and velocity behaviour at the current position, it is nearly impossible to extrapolate this information to a larger area due to strong non-linear processes. The dynamic impact of higher harmonics is not always reproduced by the numerical model due to both coarse grid resolution and numerical limitations. Among these, the missing

wetting/drying option plays a major role (e.g., Stanev et al., 2016). It is also clear that, in a region such as the SRB, the quality of the bathymetry and the resolution of its features are the key points for realistic model calculations of the hydrodynamics and sediment transport. To our knowledge, the best spatial resolution among the available numerical simulations of the area is 100 m (Purkiani et al., 2015). This study investigates tidally induced dynamics in the SRB based on the FESOM-C coastal numerical solution (Androsov et al., 2019) with a focus on the non-linear dynamics. The FESOM-C model works with triangular, rectangular and mixed meshes and is equipped with a wetting/drying option. This allowed us to resolve the dynamics in the intertidal zone carefully. There have been several studies of the Lister Deep, the Lister Ley, and the Højer and Rømø Deeps in recent years (Mielck et al., 2012, Boldreel et al., 2010). Based on these, we have created a new bathymetric map for the area. For this new bathymetric product, it made sense to work with high resolution grids (up to 2 m in the wetting/drying zone). We have studied the evolution of the tidal energy in the domain in detail by providing residual circulation and tidal ellipse maps, defining the role of higher harmonics in the dynamics and by suggested and realized tidal-wave asymmetry analysis. We have not only concentrated on M2 wave-induced dynamics but have also prescribed the elevation generated by the sum of M2, S2, N2, K2, K1, O1, P1, Q1 and M4 harmonics at the open boundary. The main motivation is that M2 accounts for only 60 % of the tidal potential energy entering the domain based on available tidal atlases (e.g., TPXO 9). A great deal of attention has been paid to the choice of open boundary conditions, model verification against available tide gauges as well as against recent ADCP data, and behavior of the solution on different grids. The last item is important because, if we are sure the results converge, then further increasing the resolution will not lead to substantially different results. We also showed the intertidal zone and updated the tidal prism value. The results of the paper gives a necessary base for the analysis of the velocity behavior, water parcel trajectories and bedform peculiarities in the area.

The manuscript is organized as follows. The 'Model Setup' section contains information about the numerical ocean solution, the grids, the open boundary conditions and the bathymetric data we used. The next section contains information about the observational data we used to verify the simulations. The 'Results' section contains model validation results and detailed information about tidally induced barotropic dynamics in the area, with a focus on the nonlinear dynamics. The 'Discussion' section contains information about possible sediment dynamics outputs based on our results, and about grid performance. The last sections summarize the manuscript and provide the supplemental data.

2 Model setup

2.1 Coastal numerical solution

FESOM-C is a coastal branch of the global Finite volumE Sea Ice Ocean Model (FESOM2, Danilov et al, 2017). FESOM-C has cell-vertex finite volume discretization and works on any configurations of triangular, quadrangular or hybrid meshes (Androsov et al., 2019; Danilov and Androsov, 2015). It has split barotropic and baroclinic modes and a terrain-following vertical coordinate; and it is equipped with 3rd-order upwind horizontal advection schemes, implicit 3rd-order vertical

advection schemes, implicit vertical viscosity, biharmonic horizontal viscosity augmented to the Smagorinsky viscosity, and the General Ocean Turbulence Model (GOTM, Umlauf and Burchard, 2005) for the vertical mixing. The wetting and drying of intertidal flats have been included because this is a crucial point for the reconstruction of the non-linear dynamics in the shallow zone.

All results except inter-comparison of the different tidal solutions are obtained based on multi-layer barotropic simulations. In all simulations only tidal forcing was turned on. The 10-sigma (terrain-following) vertical layers were prescribed. The distribution of the sigma layers satisfies the parabolic function with the crowded of the layers near the surface and near the bottom. The minimum possible thickness of the vertical layer is ~1 cm. The k-epsilon turbulence closure was applied. The choice of the bottom friction coefficient and roughness height for the depth-averaged and multi-layer simulations correspondently is described in the Section 4.1 (Results. Model validation). To avoid errors due to the inconsistency between the character of equations and the specified open boundary conditions (prescription of the tidal elevation only), a 3-km sponge layer has been introduced (Androsov et al., 1995). It gradually turned off the advection of momentum and viscosity in the vicinity of the open boundary.

The spin up period duration was determined by the total energy stationary case and was about 3 months. For the analysis we considered two last lunar (synodic) months (59 days). We simulated the tidal dynamics in 2018, which is expressed in Doodsen correction of the prescribed amplitudes and phases at the open boundary, therefore we were able to compare simulated and observed velocities second to second.

Unless otherwise indicated, the figures visualize depth-averaged behavior.

2.2 Grids

We have created two grids for the area of interest; all simulations were performed on these two grids. One grid is curvilinear and the other is unstructured and contains mostly arbitrary quads with a few triangles.

The curvilinear grid contains 119305 nodes; the resolution varies from 14 to 261 m. The finest resolution is in Lister Deep near the southwestern boundary and in the eastern area of the internal part of the domain. The curvilinear grid was generated by the elliptic method (Thompson, 1982).

The unstructured grid contains 208345 nodes (10398 triangles; 201141 quads); its resolution varies from 2 m in the wetting/drying zones to 304 m in the deepest area of the external (seaward) part of the considered domain (Fig. 1). The size of grid cells is determined by the information about the bathymetry, the bathymetry gradient and the zones of particular interest (Lister Deep; main draining channels). The unstructured grid was built using the mesh generation software package of the Surface Water Modeling System (SMS version 12.3, AQUAVEO).

Both grids have nearly the same open boundary position. The nodal areas at both grids are presented in the Appendix (Fig. A1).

2.3 Open boundary conditions

We relied on four sources for the open boundary conditions of the tidal elevation: TPXO 8.1 and 9 (Egbert et al., 2002); the output of NEMO (Nucleus for European Modelling of the Ocean, Gurvan et al., 2017) simulations for the North-West European Shelf (Copernicus Marine database); and FES2014 (Finite Element Solution 2014, Carrere et al., 2016).

TPXO 8.1 and 9 are fully-global models of ocean tides which best-fit, in a least-squares sense, the Laplace Tidal Equations and altimetry data. They provide information about 13 harmonic constituents (or 15 with TPXO 9). TPXO 8.1 and 9 atlases are combinations of the 1/6° base global solution and the 1/30° resolution local solutions for all coastal areas including our domain of interest. Each subsequent model in TPXO is based on updated bathymetry and assimilates more data than previous versions.

The European north-west shelf model results include information about hourly instantaneous sea level. The sources are full baroclinic simulations based on version 3.6 of NEMO with data assimilation (vertical profiles of temperature, salinity, and satellite sea-level anomaly). The model is forced by lateral boundary conditions from the UK Met Office North Atlantic ocean forecast model and, at the Baltic boundary, by the CMEMS Baltic forecast product. Information about the tidal constituents we obtained by performing an FFT (Fast Fourier Transform) analysis of the elevation signal at our open boundary based on data for one year (2017).

FES2014 is a global finite-element hydrodynamic solution with assimilated altimeter data and a grid resolution of 1/16° x 1/16°. FES2014 is the latest version of the FES (Finite Element Solution) tide model; it was developed from 2014 to 2016 and provides a solution for the 34 main constituents.

2.4 Bathymetric data

Bathymetric data for a given area were generated based on two sources: the AufMod database (Valerius et al. 2013), with a 50 m resolution for the whole area; and newly obtained data for the inlet and the main tidal channels, with a grid resolution of 10 x 10 m. The high-resolution part was not modified; the transition zone between coarse and fine bathymetric data was smoothed by various convolution filters.

The new bathymetric data in Lister Deep tidal inlet and the main tidal channels was obtained during winter of 2017-2018 using the hull-mounted ELAC SeaBeam 1180 multibeam system on board the RV “Mya II” of the Alfred Wegener Institute. The data were collected at sub-meter resolution and resampled to a gapless 10 x 10 m grid for the purpose of this study. The multibeam survey was intended to cover areas with water depths of mainly > 5 m in the tidal inlet and the main tidal channels. Data on the depth of areas of shallow water (< 5 m) or that were otherwise inaccessible to the vessel were obtained from the AufMod database (Valerius et al. 2013) and used with a spatial resolution of 50 x 50 m.

3 Observational data for model validation

3.1 In-situ currents and wind data

The observed velocities represented the base for validation of the model and testing of the different tidal open boundary conditions. The data set is composed of observed profiles of the water currents gathered on five cruises of the RV "Mya II" (https://doi.pangaea.de/10.1594/PANGAEA.894070). The transects cross Lister Deep perpendicularly in two positions: for outer part, at the narrowest and bathymetrically simplest part of the inlet and for the inner part, because the entire water volume has to pass through this transect; and at the entrance areas to the three main tidal channels (Fig. 1). The cruises were conducted between May 22 and May 30, 2018; observations were carried out for half and whole tidal cycles (Table 1). The data were collected using a Teledyne RDI WorkHorse 600 kHz ADCP (Teledyne RD Instruments, San Diego, USA) mounted in the moon pool of the RV "Mya II" (of the Alfred-Wegener-Institute) with an offset of 1.3 m related to the water surface. In addition, a differential GPS with a motion sensor worked together with the ADCP to refine and correct the velocity measurements regarding the heading, pitch and roll movements of the ship. Here we would stress that the surveys were conducted during different tidal periods (Table 1), which is crucial for high-quality verification.

Wind data were automatically measured by an anemometer mounted on the RV "MYA II" (summary of the wind conditions can be found in the Appendix, Table A1); the data were obtained from the DAVIS SHIP database for the time of the cruises. The main wind direction during the cruises was around 90° (east); the most frequent intensities were in the range of 5 to 10 m/s. On May 24 the wind was blowing strongly from the east for nearly the whole cruise. Exceptions concerning wind direction were the cruise on May 23, when winds were from the NNW (330°), and the cruise on May 29, when the most frequent intensity ranged between 10 and 15 m/s.

3.2 Tide gauge (TG) data

The tide gauge data for the area are represented by three stations: List TG (8.441°E; 55.017°N), Vidå TG (8.667°E; 54.967°N) and Havneby TG (8.565°E; 55.087°N) (Fig. 1). All data were downloaded from the EMODnet database (the European Marine Observation Data Network Seabed Habitats project (www.emodnet-seabedhabitats.eu)), which is funded by the European Commission's Directorate-General for Maritime Affairs and Fisheries (DG MARE) and provided by the Waterways and Shipping Office in Tönning, the Danish Meteorological Institute and the Danish Coastal Authority. For the spectral analysis, we used data with a 10-minute resolution covering the time period from the middle of 2014 through the end of 2017. The time of the observations is the UTC (+0) zone.

4 Results

4.1. Model validation

Model validation was organized into the following two steps: (1) selection of the best open boundary conditions using ADCP data and (2) validation of the best open boundary solution against existing tide gauge data, in particular using List TG, Vidå

TG and Havneby TG data. For step (1), the measurements were done during different tidal periods (spring, neap, ebb, and flood) in the area of Lister Deep and the main inlets (Fig. 1), which are characterized by the largest depths (up to 35 meters) in the domain and by the highest as well as by complex tidally induced velocities. We performed the frequency analysis using the MATLAB-package T-TIDE (Pawlowicz et al., 2002) and identified the errors in amplitude and phase for the main tidal constituents (with maximum amplitudes), including higher harmonics.

Table 2 represents the Root Mean Square Deviation (RMSD) and correlation coefficients of the observed velocities (ADCP data) and the modelled velocities obtained for each open boundary solution. The comparison is based on depth-averaged velocities since the measurements were performed in the deep part of the domain and our task here was to check the performance of the different tidal forcing. In Table 2, results for all the open boundary solutions we used are shown only for the first grid since the difference between the results on different grids is $\leq$ 0.01 for correlation coefficients and $\leq$ 0.01 m for the RMSD. However, we would note that the unstructured grid provides slightly better results despite its somewhat coarser resolution (the unstructured grid has a larger number of cells, mainly due to detailed representation of the wetting/drying zone). Based on additional experiments (Kuznetsov et al., 2019), we think the reason is that the unstructured grid reflects the bathymetric gradients.

We used different bottom-friction coefficients (C_d) for the different tidal solutions. However, for each run C_d was spatially uniform as soon as the seabed habitat map is not available yet for the considered area. At the beginning, we took the C_d coefficient as equal to 0.0025 for all simulations. The NEMO solution got much worse results in this case than presented in Table 2 in terms of the RMSD and correlation coefficient (RMSD is larger on average by 15%, correlation coefficient is less on average by 5 % and 6 % for u and v component respectively). Further analysis showed that the predicted velocities for the NEMO open boundary solution are too large during some tidal phases. We therefore decided to vary the C_d in a range from 0.002 to 0.004, taking into account the largely sandy bed in the domain, to reach the best agreement with observations (e.g., Werner et al., 2003). Finally, for the TPXO solutions, we used a C_d equal to 0.0025; and for the NEMO solution, a C_d equal to 0.0035. Note that smaller or larger coefficients did not improve results in terms of RMSD and the correlation coefficient.

Table 2 shows that the TPXO 9 solution fits the ADCP data best; second best are the TPXO 8.1 and NEMO solutions; and then the FES 2014 solution follows. For all solutions except FES, the correlation coefficients are higher during spring tides as well as in the deepest part of the domain; this is true in particular for the measurements performed on May 29 and May 30 and despite the quite strong winds often ranging from 10 to 15 m/s (Table 1, Fig. 1). On May 23 and May 24, the measurements were performed on nearly the same side; but the May 24 correlation coefficient for the 'v' component is relatively small. This can probably be explained by the permanent wind from the east. We can conclude that tides in that zone explain, on average, more than 80 % (or 90 % or more in case of a spring tide) of the dynamics in case of absent storm (more than 20 m/s) and blowing continuously in one direction winds. Likewise we conclude that it would be impossible to judge open-boundary-condition quality using information from only one cruise. Figure 2 represents observed and modelled depth-averaged velocities on May 29 (a spring tide). Figure 2 clearly illustrates how the different solutions can align closely

at one moment and then begin to deviate greatly at another. Furthermore, the largest velocity errors for all solutions occur when tidal velocities are small as well as during the tidal state change (see e.g., in Fig. 2, the time from 7 a.m. to 8 a.m. or from 1 p.m. to 2 p.m.). This is quite logical, because other effects such as baroclinicity, wind impact, and their non-linear interactions then become more pronounced. However, TPXO 9 shows the best agreement with observations during slack tide and provides the smallest RMSD among suggested solutions for all observation days (Fig. 2).

Despite the quite good results of TPXO 8.1 (Table 2), the unstructured grid yields a number of vortex structures near the open boundary that cannot be removed by the sponge layer, which dumps advection and diffusion near the open boundary. It is known that grids that employ an arbitrary normal at the open boundary are subject to the quality of the open boundary signal (Danilov and Androsov, 2015). For TPXO 8.1, the behaviour of the phase is not realistic near the solid boundary: the phase goes through zero simultaneously near the western and eastern solid boundaries.

Once we determined the best open boundary conditions solution—TPXO 9, based on ADCP data—we moved on to the second verification stage. For this, we switched to a 3D-simulation with 10 vertical layers, which are crowding near the sea bed. The optimal roughness height was 0.001 m; this value agreed with one estimated from observations in a similar region (Werner et al., 2003) and, in terms of the mean, with a Cd equal to 0.0025 for the 2D-scenario. Table 3 presents the results of the frequency analysis of the observational data from the List, Havneby and Vidå TGs as well as from the model using TPXO 9 open boundary conditions (Taylor diagrams can be found in the Appendix, Fig. B1). Here we present results from both of the grids under consideration. The observed phase values are quite often situated between the values given by the solution on the different grids. This is because we used nearest-to-the-observational-point grid nodes to perform the analysis, and did not interpolate the values to the particular coordinates. Either solution (per grid) performed well; but each slightly underestimated the amplitudes for major diurnal and semidiurnal constituents (except for the M2 amplitude at the Vidå TG). Note that the M2 tidal wave and its subharmonics are shown to vary in amplitude and phase on seasonal, annual, and secular time-scales (Müller, 2012, 2014; Woodworth et al., 2007; Gräwe et al., 2014). The annual variations of the M2 amplitude are between 6 and 11 % of the annual mean amplitude for the shallow water stations; the phase can vary by 2 to 6° persistently over the last century (Gräwe et al., 2014). The summer amplitudes seem to be larger than the winter amplitudes; this can be explained by changes in thermal stratification (Müller, 2012, 2014; Gräwe et al., 2014). Our simulations obtain "winter" amplitudes, while the observational data provide a mean annual amplitude. The M4 constituent also has a noticeable phase error of ~30° at all stations. But due to large bathymetric uncertainties in the area of the stations, such an inaccuracy is hard to correct (here, the resolution of the bathymetry we used is 50 m). Note that at the Vidå TG, the unstructured grid shows significantly better agreement than the curvilinear grid. This is not surprising since the unstructured grid has much better resolution there.

4.2 Wetting/drying, maximum tidally induced velocities and tidal prism

Figure 3a shows the probability, in the unstructured grid case, of each node being wet with tidal forcing alone. This figure is based on simulation results for two lunar (synodic) months (29.5 days × 2) after the model reaches a periodic regime. The unstructured grid more accurately represents the wetting/drying zone; it can be traced in smoother forms and in smaller-scale detail than in the curvilinear grid (not shown).

An extensive intertidal subarea situated in the western and southern parts of the considered domain as well as in the in the Königshafen embayment can be seen; and the Jordsand creates a secondary bight with the Rømø Deep main channel (Fig. 1, Fig. 3a).

Figure 3b shows the maximum velocities at each grid point within a lunar (synodic) month. Thus, Fig. 3b shows the highest possible tidally induced velocities in the domain. Figure 3b exhibits, as expected, a correlation with the depth (Fig. 1); but there are many peculiarities, which emphasize the large role of non-linear processes in the domain. The maximum velocities can be found at the opening of Lister Deep and near the edge of Sylt during spring ebb and are ~1.98 m/s. The tidal prism for the bight varies from 3.3 to 6.5 × 10^8 m, with a mean value of 4.8 × 10^8 m; the tidal prism for the whole area varies from 5 to 10 × 10^8 m, with a mean value of 7.5 × 10^8 m.

4.2 Energy balance

The analysis of the energy budget and energy flux distribution provides an important insight into the evolution of energy in the modelled region. The energy balance for the vertically averaged equations for the barotropic case has the following form (see, e.g., Androsov et al., 2002):

$$\frac{\partial \bar{E}}{\partial t} + \nabla \cdot \left[\rho H \left(g\xi + \frac{1}{2}|\bar{\mathbf{v}}|^2 \right) \bar{\mathbf{v}} \right] = -\rho C_d |\bar{\mathbf{v}}|^3 + \rho \bar{\mathbf{v}} \cdot \left(\nabla \cdot (KH \nabla \bar{\mathbf{v}}) \right), \quad (1)$$

where $\bar{E} = \frac{1}{2}\rho(H|\bar{\mathbf{v}}|^2 + g\xi^2)$ is the total energy per unit area, $\bar{\mathbf{v}} = \int_{-h}^{\xi} \mathbf{v}\, dz$ is the vertically integrated fluid velocity, $\mathbf{v} = (u, v)$, ξ is the sea surface elevation, h is the water depth, $H = h + \xi$ is the full water depth , ρ is the water density, C_d is the bottom drag coefficient, K is the horizontal eddy viscosity coefficient, g is the acceleration due to gravity and $\nabla = \left(\frac{\partial}{\partial x}, \frac{\partial}{\partial y}\right)$ is the nabla operator. Note that we did not introduce horizontal viscosity into our equations; therefore K equals 0 in our simulations, and further this part of the balance will be omitted. After integration of eq. (1) over the region Ω with boundary $\partial\Omega = \partial\Omega_1 + \partial\Omega_2$, where $\partial\Omega_1$is the solid part of the boundary and $\partial\Omega_2$ is the open boundary, taking into account the Gauss formula for divergence and the condition of zero velocities at $\partial\Omega_1$, we obtained the following mean energy balance equation for our depth-averaged solution:

$$\int_\Omega \frac{\partial \bar{E}}{\partial t}\,dx\,dy = -\int_{\partial\Omega_2}\left[\rho H\left(g\xi + \frac{1}{2}|\bar{\mathbf{v}}|^2\right)\bar{\mathbf{v}}\cdot\mathbf{n}\right]ds - \int_\Omega \rho C_d|\bar{\mathbf{v}}|^3\,dx\,dy\,, \quad (2)$$

where $\mathbf{n}$ is the outward normal to $\partial\Omega_2$.

The first term on the right side of (2) is the total flux of energy across the open boundary, and the second term is the rate of energy dissipation due to the bottom friction. Figure 4 shows the energy balance for the whole area based on unstructured grid for the summary tide for one M2 period (the energy balances for the whole area at both grids are visually identical). Once we have different diurnal and semidiurnal constituents in the system, the energy balance every M2 period will not be the same. However, Fig. 4 demonstrates the overall picture. The total energy in the area varies between 7×10^{11} to 3.5×10^{12} J on both grids (in the case of TPXO 8.1 conditions, the total energy in case of unstructured grid had different variation limits). For comparison, the full tidal energy in the modelled area is almost equivalent to the full energy of the barotropic tidal dynamics in the Strait of Messina (Androsov et al., 2002), and one order of magnitude less than in Bab el Mandeb Strait (Voltzinger and Androsov, 2008). The potential energy is one order of magnitude larger than the kinetic energy. The shares of the total energy based on the open boundary information are distributed in the following way: M2 brings 58 %, S2 - 13.5 %, N2 - 10 %, K2 - 3.5 %, K1 - 4 %, O1 - 5.5 %, P1 - 1 %, and the Q1 and M4 components bring 1.5 % and 3 % correspondingly. The fluxes through the open boundary can remove up to 1.5×10^8 J per second. Bottom friction takes up a significant amount of energy, on average 6.4×10^7 J per second, due to the shallowness of the bight (Fig. 4). The imbalance is two orders of magnitude smaller than the energy change. The unstructured grid is a bit more dissipative; its imbalance is 10 % larger than that on the curvilinear grid. This is for several reasons: the unstructured grid in particular contains triangles, arbitrary quads and, in some places, large gradients in grid cell size, which causes additional noise (Danilov and Androsov, 2015). We would point out that it is hard to estimate the numerical dissipation rate precisely. The current imbalance consists not only of numerical dissipation but also of uncertainties in the energy balance calculation once we no longer accounted for the role of the explicit time-difference scheme with an Adams–Bashforth extrapolation and the effects of velocity filtration. Our additional runs showed that the impact of these procedures has the same magnitude as a calculated imbalance. We think that, on the curvilinear grid, the "real" imbalance due to numerical viscosity is close to zero, at least one magnitude smaller than the presented one.

The maximum change in system energy and maximum fluxes through the open boundaries take place during ebb tide; the ebb phase duration is, on average, 0.85 of the flood phase. These general conclusions mask very patchy dynamics in the area, which are considered in detail in the next sections.

Figure 5 demonstrates the energy fluxes in the area. The tidal energy flux, represented by the sum of the potential and kinetic energy fluxes, is estimated using the following definition (Crawford, 1984; Kowalik and Proshutinsky, 1993):

$$(E_\lambda, E_\theta) = \frac{1}{T}\int_0^T \rho H\left(g\xi + \frac{1}{2}|\bar{\mathbf{v}}|^2\right)\bar{\mathbf{v}}\;dt, \quad (3)$$

where E_λ, E_θ are the zonal and meridional components of the tidal energy flux vector, and T is the full tidal period (sinodical month - 29.5 days). Figure 5a, b, and c show that the potential energy fluxes in the area are one order of magnitude larger than the kinetic energy fluxes. Therefore, total energy fluxes are largely defined by potential energy fluxes (Fig. 5b, c). It can be noted that the directions of the potential and kinetic energy fluxes can deviate from each other and be opposite (Fig. 5a, b); this is can be explained easily by the fact that the kinetic energy fluxes largely reflect dissipation of the energy, and the potential energy fluxes largely reflect energy distribution pathways in the domain. So, in Fig. 5b and c, it can be seen that the dynamics in the external part of the domain is determined by the Kelvin wave coming from southwest. Obviously, the bulk of the energy comes into the internal part of the domain through Lister Deep. The energy leaves the whole modelling domain mostly through the north-eastern part of the open boundary. Figure 5d demonstrates that the bulk of the energy comes to Königshafen from the south and there circulates through the system of gyres (the curl part of the energy fluxes is larger than the divergence part). Figure 5d also indicates that the energy fluxes along the coastline in this subarea are opposite in direction to those within the main channel.

4.3 Residual circulation

The residual circulation in the area is characterized by the large number of vortex structures with different rotation directions in the area of Lister Deep and the main channels (Fig. 1, 6a). Note that the residual circulation in the external part of the domain is defined by kinetic energy fluxes, because here the role of nonlinearity in the continuity equation is minor (the water depth compared to the tidal amplitude is relatively large). These vortexes organize a complex residual circulation pattern; the strongest circulation (up to 0.45 m/s) can be found in the area of Lister Deep, where different incoming and outgoing flows meet, and in the other areas of large bathymetric gradients. Note, that the two largest vortex structures in terms of the residual velocities magnitude, which show opposite rotational, were also resolved by Burchard et al. (2008) and Ruiz-Villarreal et al. (2005) based only on the M2 signal. Near Königshafen we can also follow the gyre system in the opposite direction, which alternates (Fig. 6b). Note that, here, the energy fluxes and residual circulation patterns have much in common. The bulk of the energy fluxes come from the south, and tides lose energy on the way, causing residual circulation shaped by the bathymetric features. For this subarea, the residual velocities are less than 0.05 m/s. The residual circulation in the external part of the domain shows that the bulk of water masses penetrate to the internal part of the domain from the western boundary and the south, moving along the coast. Water masses mainly leave the domain through the central part of the open boundary. Such a complex residual circulation (Fig. 6) signals potential difficulties in calculating sediment budget.

4.4 Tidal ellipses

The resulting movement in the SRB represents a superposition of the tidal waves reflected off the region's solid boundaries. As a result of this interference, a standing wave occurs, containing only one component of the velocity for the main tidal harmonics, which is to say: currents are close to reverse. The Coriolis effect does not lead to significant cross-currents.

Figures 7a and 7b show the ellipses of the wave M2 and S2 tidal currents, respectively; the character of the currents of either wave component is practically indistinguishable in the SRB except for the amplitude of the M2 velocity, which turned out to be almost four times larger than the amplitude of the S2 velocity. The direction of rotation of the velocity vector is determined by the sign of the ellipticity. A negative ellipticity value means that the tidal current vector rotates anticyclonically. The anticyclonic rotation of the depth-averaged velocities near Sylt-Rømø is inherent only in zones of a significant bathymetric gradient where maximum tidal currents are observed. This kind of rotation has to overcome the Coriolis effect, which spins in the opposite direction. At the same time, on the boundary with the North Sea (the open boundary of the modelled region), the currents have a constant cyclonic rotation, which corresponds to the cyclonic movement of the Kelvin wave along the coast in the Northern Hemisphere.

The ellipses induced by the M4 wave are shown in Fig. 7c. This picture differs from the main tidal harmonic frequencies in the presence of mixed flow zones. In deep-water channels, the currents are close to reverse during the tidal cycle; and on the shape of bathymetry the transverse velocity component appears. The amplitude of the velocity of the M4 wave reaches 25 cm/s in most bottlenecks of the modelled region and near Königshafen. Near the open boundary, the currents have a pronounced anticyclonic character, i.e., nonlinear flows overcome the Coriolis effect, spinning the flow in the opposite direction. In some areas around the shallow zones, the major axis of the M4 ellipsis is at a significant angle to the major axis of the M2 ellipsis. This can lead to secondary circulation in a rotating system.

4.5 Nonlinearity structure and tidal asymmetry

The major higher harmonics in the area are M_4 with 36.6 % of total energy attributed to the nonlinear harmonics in the whole considered domain, M_6 - 12.43 %, MS_4 - 12.27 %, MN_4 - 10.95 %, M_8 - 6.43 %, $2MS_6$ - 5.6 %, $2MN_6$ - 5.23 %, MO_3 - 4.73 %, SN_4 - 4.08 %, S_4 - 0.92 %, $2SM_6$ - 0.75 %. These numbers were calculated based on a weighted sum of the harmonic amplitudes. Figure 8 shows the relative role of these higher harmonics compared to the M2 signal and the tidal map for M2 wave. In particular, Fig. 8a demonstrates the ratio of the M2 amplitude to the sum of amplitudes of the listed higher harmonics. The role of nonlinear harmonics becomes significant in the interior zone of the domain, increasing with greater distance from the bottleneck and near the wetting/drying zone (Fig. 3a, Fig. 8). To quantify the role of the higher harmonics, Fig. 8b also demonstrates the tidal map for the M2 wave. The M2 wave amplitude is greatest in the southern part of the internal area. Also, we have one degenerate amphidromic point in the external part of the domain defined by capture of the Poincare wave.

The domain configuration and the foregoing results of the tidal energy transformation and evolution are signals of a pronounced tidal asymmetry in the tidal water level and in the current velocity behavior in the area. There are several reasons for the tidal asymmetry—in particular, the presence of the non-linear advection and bottom friction terms together with complex topography, resulting in a non-trivial wave interaction in the system (e.g., Friedrichs and Aubrey, 1988). The key geometric features directly impacting tidal distortion are the bathymetry relative to the tidal amplitude, the “bottleneck”

width and its variation during the tidal cycle, and the area occupied by the intertidal zone and its distance to the main tidal inlets. For data about tidal asymmetry to inform sediment dynamics analysis, we concentrate on the ebb and flood durations as well as the mean and maximum velocities relations. Ebb is defined as a period when the water level at the current location is decreasing, and flood as the period when it is increasing. Figure 9a (left panel) represents the ratio between the maximum velocities during spring ebb and flood. Figure 9b (left panel) represents the ratio of mean velocities during ebb and flood periods. Figure 9c (left panel) represents the ratio of mean ebb and flood durations. The analysis reflects near-bottom velocities; however, the pattern of ratios is nearly the same for the depth-averaged solution. We note generally that the near-bottom solution provides a more pronounced ebb or flood dominance. The features represented in Fig. 9 (left panel) show the *mean pattern* for a lunar (synodic) month (29.5 days). In such a domain, we can expect that the flood-ebb dominance feature is not constant but can change within a lunar (synodic) month. For some ebb-flood cycles, the picture presented in Fig 9 (left panel) can be significantly different. Therefore, we have decided to calculate how often flood or ebb dominance takes place within a lunar (synodic) month in terms of velocities and duration.

Figure 9 (right panel) comprises 57 floods and ebbs. (We considered 28.5 days, but the "first" and "last" flood and ebb of the lunar (synodic) month —29.5 days—were removed to make sure that we were considering the beginning of the flood and ebb.) Then we calculated how often the mean and maximum velocities of the ebb are larger during the following flood (Fig. 9a, b right panel). We also calculated how often the ebb duration was smaller than that of the following flood (Fig. 9c, right panel). In other words, Fig. 9a (right panel) shows for example the frequency of the maximum velocity during ebb being larger than that of the following flood; a value of 57 means that across all 57 cycles, maximum velocities during ebb are larger than during flood. We should note, that flood or ebb dominance is caused not only by non-linear effects, but also due to diurnal inequality of tide. From all these pictures, we have removed subareas which did not take part at least at one flood-ebb cycle.

Figure 9 was generated from simulations on the curvilinear grid. But an important result is that the difference between the ratios (asymmetry indicators) on either grid touches only a few details, but not a general pattern. The maximum disagreement occurred during comparison of the ratios of velocities, going up to 0.2 for ratios of mean and maximum velocities. However, we would stress that the position of the ebb/flood dominance areas are the same with only a small difference at the edge of the zones.

The patterns presented in the left and right panels show some common features, and this is to be expected. For example, if the ebb velocities are larger than the flood velocities nearly every ebb-flood cycle, then the **averaged** value of the velocity ratios will be large, and the corresponding figure in the right panel will show a high frequency of the ebb-dominance event. Figure 9 (right panel) shows that there are a lot of zones that may behave differently during different periods of a lunar (synodic) month. (The frequency is between 0 and 57.) Note also that Fig. 9a and 9b represent largely different patterns than Fig. 9c. For, example, if the mean and maximum velocities in the internal part of the domain are larger during flood, it does not mean that the flood will be shorter. There can be no mass conservation for the ebb-flood cycle for the particular area

subunit. Note that the ebb in the whole domain under consideration is typically shorter than the flood, except in the south-western part of the internal area (Fig. 9c, left panel).

Figure 9 demonstrates that it is not correct to regard ebb or flood dominance based only on velocity characteristics or typical flood/ebb durations when these characteristics can yield opposite answers. Additionally, these characteristics are not necessarily the same within one lunar (synodic) month (29.5 days).

To explain the complexity of the presented pattern, we have split the domain under consideration into four parts designated as zones 1 through 4 (Fig. 9a, left panel).

4.5.1 Zone 1

Zone 1 represents an area where we observe a progressive Kelvin wave (Fig. 5, 9). The flood-dominated (orange-colored) zone, in terms of maximum velocities (figure 9a, left panel), matches the area where we have a comparatively small residual circulation (Fig. 6). Gravity waves traverse the shallow zone nondispersively at a speed defined by $\sqrt{gH}$ (g is acceleration due to gravity, H is the full depth); so we suggest that the crest of the tide overtakes the trough here (e.g., Dronkers, 1986; Hayes, 1980; Saloman and Allen, 1983). This is confirmed by Fig. 9a (right panel), which shows that maximum velocities in this zone are nearly always larger during flood. Figure 9b (left panel) shows that mean velocities in this subzone are nearly equal to each other in terms of the mean, with slight ebb dominance. However, also some tidal cycles exhibit larger mean flood velocities than mean ebb velocities (Fig. 9b, right panel).

4.5.2 Zone 2

In zone 2, we have an extensive intertidal zone and maximum amplitudes of the semidiurnal tides compared to other zones; also, this zone lies far from the Lister Deep area. In this zone, the role of higher harmonics is greatest (Fig. 8), revealing the major role of non-linear friction effects and non-linearity in changes of the water-layer thickness: here, the ratio of tidal amplitude to depth is greatest (increasing from Lister Deep toward the southern part of the zone). This is also can be seen in Fig. 7, which shows M4 locked in a velocity phase of -90º to 90º relative to M2. As a result, water level changes propagate more slowly during ebb (Dronkers, 1986), and the time-delay between low water at the inlet to Lister Deep versus in the considered area is greater than that for high water. In every regard, the father away from Lister Deep, the more pronounced the flood dominance becomes. This means that ebb duration increases, and velocities are larger during flood.

4.5.3 Zone 3

In zone 3 we have very patchy dynamics in terms of velocities during flood and ebb (there are a lot of subzones characterized by the flood dominance and ebb dominance); however, it is typical for the whole area that ebb is shorter than flood (flood duration is between 1.1 and 1.3 of ebb duration). Lister Deep can be characterized generally by higher mean and maximum velocities during ebb; but some side channels can be characterized by higher velocities during flood. As the tide turns at low water, strong currents are still flowing seaward out of the main ebb channel. As the water level rises, the flood

currents seek the path of least resistance around the margin of the delta. This creates horizontal segregation of flood and ebb currents in the tidal channels for a time. This is apparent in Fig. 10, depicting the transitional moment from ebb to flood.

In this zone, we emphasize subareas A and B as prime examples of the subdomains where mean currents ratio and maximum currents ratio (Fig. 9a, b) are not synchronized with the durations ratio (Fig. 9c). For example, Fig. 9a and 9b demonstrate that the velocities at B are larger during flood in terms of the mean and maximum; but flood duration is longer than ebb. This signals that the water parcels are travelling different pathways during flood and ebb.

4.5.3 Zone 4

Zone 4 represents a small, semi-enclosed bight with a flood-dominated main channel and an ebb-dominated area around, and in the inner part of the bight in terms of velocity. However, we would stress that flood dominance, though typical, is not a constant feature. For several cycles within a lunar (synodic) month (29.5 days), the mean and maximum velocities will be larger during ebb. For the whole zone, ebb is shorter than flood for almost a lunar (synodic) month. The reason the pattern is opposite to that of zone 3 lies in the small volume of intertidal storage and large variation in the "main channel" width. In this zone, frictional drag is insignificantly greater at low water than at high water. Also, the role of M4 tide compared to M2 tide is greatest there (not shown); the role of the sum of all non-linear harmonics is smaller than in zone 2 (Fig. 8). For this zone, ebb and flood generally start on the sides of the main channel Rømø Deep in marginal ebb-dominated channels.

5 Discussion

5.1 Bedform peculiarities

The most interesting question for future study is how the given asymmetry and residual circulation pattern line up with the bedform peculiarities. Therefore the next step will be intercomparison between measurements in frame of the planned multibeam echosounder surveys and results of the current paper. The prediction of the bedform pecularities in the area requires a coupled sediment module as well as wind and wave forcing. However, as soon as we have shown (Table 2, Fig. 2) that tides can explain a large part (more than 80 %) of the current velocities in the area of Lister Deep, some prognoses can be made at the current stage. The results suggest the presence of subaqueous dunes with stable characteristics in areas where mean and maximum current velocities are permanently higher or lower during ebb/flood than during flood/ebb. With this definition (see Fig. 9), our results agree with those presented in Boldreel et al. (2010) and Mielck et al. (2012). In these studies conducted in the working area Lister Deep and adjacent to Königshafen, dunes of various sizes, escarpments and other erosional features were analyzed based on hydroacoustic data (seismics, sidescan sonar and RoxAnn seafloor classification system) to determine dune characteristics and orientations (and hence flood or ebb dominance) of the particular areas. Boldreel et al. (2010) state that the flood-dominated dunes are larger than ebb-dominated dunes in the area of the bottleneck. Our study reveals that, in this zone, the ebb is generally shorter than the flood (Fig. 9c), which may explain this

observation. The map of the residual circulation (Fig. 6) suggests probable directions of subaqueous dune migration where bottom currents are strong enough.

5.2 Grid performance

Each presented grid had advantages and disadvantages. The curvilinear grid offered minimum numerical viscosity but was not very flexible when it came to choosing grid cell size as compared to an unstructured grid (see also, Fig. A1, A2; Danilov and Androsov, 2015; Androsov et al., 2019). This is especially crucial in the zones of large bathymetric gradients and in the wetting/drying zones. The unstructured grid is more dissipative and more sensitive to the quality of the open boundary solutions. The reproduction of the nonlinear effects on the grids of different structure represents additional scientific question, which should be untwisted in the future.

6 Summary

This study is dedicated to tidally-induced dynamics in the SRB, with a focus on the non-linear component. The newly obtained high-quality bathymetric data supported the use of high-resolution grids (up to 2 meters in the wetting/drying zone) and elaboration of the details of tidal energy transformation in the domain. The FESOM-C model was used as the numerical tool. In preparation, different open boundary conditions for the summary tide (major diurnal and semidiurnal as well as M4 constituents) were tested for the best fit with observational data. The simulations with open boundary conditions from TPXO 9 showed very satisfying agreement with available observations. Based on 3D barotropic runs, the ellipses, energy fluxes, residual circulation and tidal asymmetry maps were constructed and analyzed for the whole area for the first time. Four zones with fundamentally different asymmetry structures were indicated during tidal asymmetry analysis. We also showed that it is not correct to talk about ebb or flood dominance based only on one velocity characteristic or typical flood/ebb durations since these indicators can yield an opposite answer. Also asymmetry indicators were not constant everywhere from one ebb-flood cycle to another.

All experiments were performed on two grids with different structures and resolution details. Energy balance fulfillment was shown for both grids. The generated maps generally showed the same pattern on both grids, which allowed us to conclude that further increasing the resolution will not lead to pronounced changes in the results. The obtained results are a necessary and useful benchmark for further studies in the area, including for work on baroclinic and sediment dynamics. It would be fruitful to pursue further research about how the obtained maps reflect bedform peculiarities in the area in order to predict bedform characteristics in the shallow zones, which are hard-to-reach places for the ship surveys.

7 Appendices

Appendix A

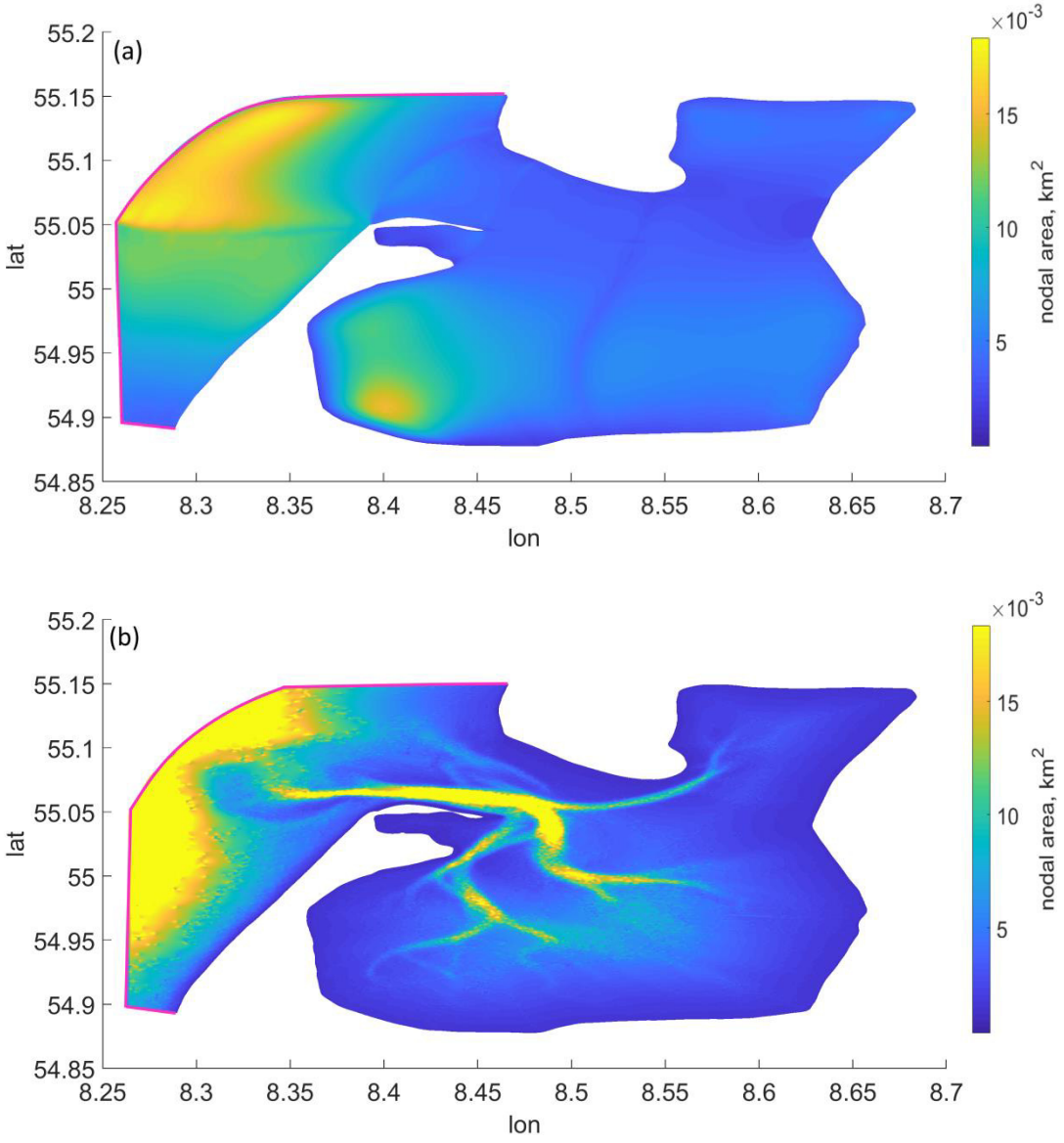

Figure A1. Nodal area, pink color indicates position of the open boundary: a) curvilinear grid; b) unstructured grid.

Table A1. Summary of the five cruises on board of Research Vessel Mya II, profiling three main transects: Inner Tidal Inlet (ITI), Main Tidal Channels (MTC) and Outer Tidal Inlet (OTI). Main Tidal Channels (MTC) show the initial, turning and ending points, since it covers three sections in one transect. The Wind Roses characterize the wind conditions during cruise times, with the legend colors representing the wind velocity in m/s and the circles representing the frequency percentage of the direction from where the wind blows.

Transect Name	Date	Lon / Lat (°) (Start – End)	Tidal Period	Duration (h)	Wind conditions (Wind Rose)
ITI	22/05/2018	8.464 / 55.047 8.489 / 55.062	neap	6:28	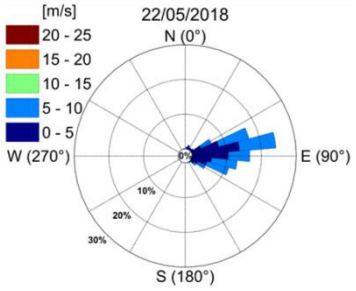
MTC	23/05/2018	8.461 / 55.039 8.474 / 55.035 8.499 / 55.046	neap+1 day	6:19	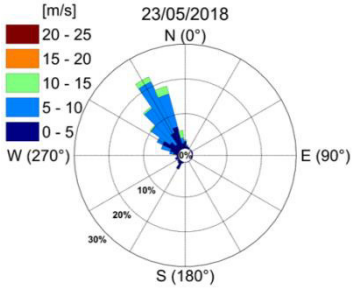
	24/05/2018	8.505 / 55.056	neap+2 days	5:56	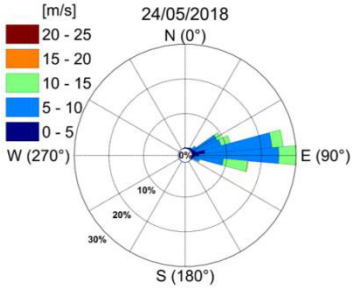
ITI	29/05/2018	8.464 / 55.047 8.489 / 55.062	spring	7:11	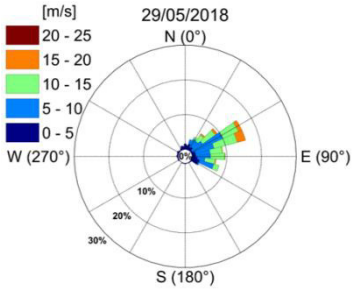

OTI	30/05/2018	8.418 55.059	/	spring+1 day	12:24	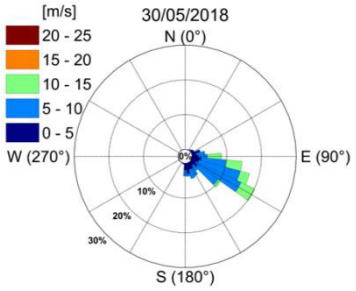
		8.428 55.071	/			

Appendix B

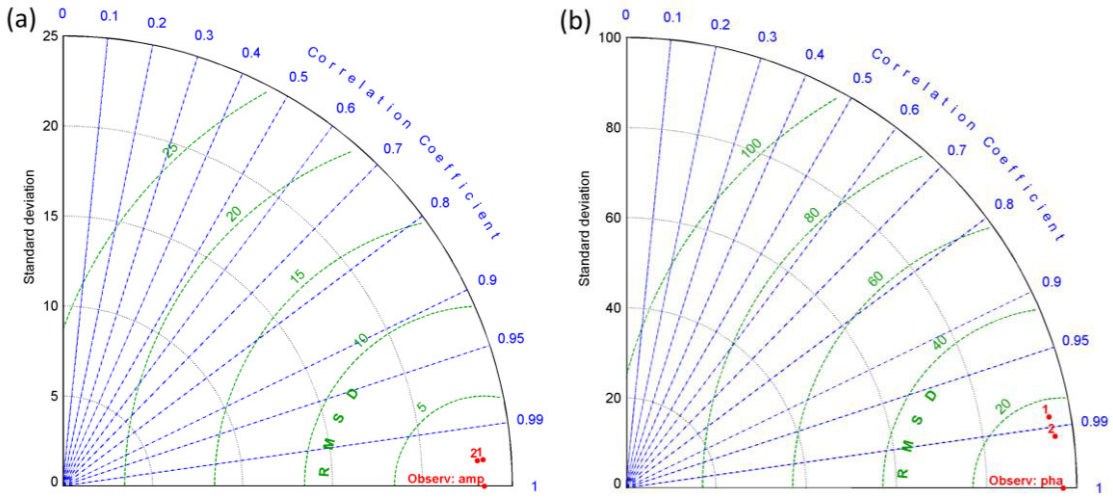

Figure B1. Taylor diagrams based on observed and modelled data at 3 gauging stations, '1' and '2' indicate simulation results on curvilinear and unstructured grids respectively: a) for amplitude; b) for phase.

Author contribution

VF designed the experiments and carried them out, prepared the unstructured grid and new bathymetry product, suggested asymmetry analysis. AA constructed curvilinear grid, encouraged FV to investigate some aspects of the nonlinear dynamics, wrote the part about tidal ellipses and helped to visualize the results. LS carried and provided the multi-beam data, participated in the construction of the new bathymetry product and consulted VF a lot during the verification stage. IK and HCH discussed with VF all experiments and results providing valuable comments and remarks. FA carried and processed ADCP data, prepared the reference list and together with HCH and LS significantly improved the manuscript readability. HCH provided the information about bedform peculiarities in the area. KHW supervised the research. All authors contributed to the final manuscript, provided critical feedback and helped to shape the research.

Competing interests

The authors declare that they have no conflict of interest.

References

Androsov, A., Fofonova, V., Kuznetsov, I., Danilov, S., Rakowsky, N., Harig, S., Brix, H., and Wiltshire, K. H.: FESOM-C v.2: coastal dynamics on hybrid unstructured meshes, Geosci. Model Dev., 12, 1009 – 1028, https://doi.org/10.5194/gmd-12-1009-2019, 2019.

Androsov, A. A., Kagan, B. A., Romanenkov, D. A. and Voltzinger, N. E.: Numerical modelling of barotropic tidal dynamics in the strait of Messina, Adv. Water Resour., 25, 401 – 415, https://doi.org/10.1016/S0309-1708(02)00007-6, 2002.

Androsov, A.A., Klevanny, K.A., Salusti, E.S., Voltzinger, N.E.: Open boundary conditions for horizontal 2-D curvilinear-grid long-wave dynamics of a strait, Advances in Water Resources, 18, 267–276, 10.1016/0309-1708(95)00017-D, 1995.

Austen, I.: The surficial sediments of Königshafen - variations over the past 50 years, Helgolander Meeresun., 48, 163–171, https://doi.org/10.1007/BF02367033, 1994.

Becherer, J., Burchard, H., Flöser, G., Mohrholz, V. and Umlauf, L.: Evidence of tidal straining in well-mixed channel flow from microstructure observations, Geophys. Res. Lett., 38, L17611, https://doi.org/10.1029/2011GL049005, 2011.

Bolaños-Sanchez, R., Riethmüller, R., Gayer, G. and Amos C. L.: Sediment transport in a tidal lagoon subject to varying winds evaluated with a coupled current-wave model, J. Coastal Res., 21, e11 – e26, https://doi.org/10.2112/03-0048.1, 2005.

Boldreel, L. O., Kuijpers, A., Madsen, E. B., Hass, H. C., Lindhorst, S., Rasmussen, R., Nielsen, M.G, Bartholdy, J. and Pedersen, J. B. T.: Postglacial sedimentary regime around northern Sylt, South-eastern North Sea, based on shallow seismic profiles. Bull. Geol. Soc. Den., 58, 15 – 27, 2010.

Burchard, H., Flöser, G., Staneva, J. V., Riethmüller, R. and Badewien, T.: Impact of density gradients on net sediment transport into the Wadden Sea, J. Phys. Oceanogr., 38, 566 – 587, https://doi.org/10.1175/2007JPO3796.1, 2008.

Canuto, V.M., Howard, A., Cheng, Y., Dubovikov, M.S.: Ocean turbulence. Part I: One-point closure model-momentum and heat vertical diffusivities, J. Phys. Oceanogr., 31, 1413 – 1426, 2001.

Carrere L., Lyard, F., Cancet, M., Guillot, A. and Picot, N.: FES 2014, a new tidal model – Validation results and perspectives for improvements, ESA Living Planet Conference, Prague, Czech Republic, 9-13 May, 2016, ESA Living Planet Symposium, 2016.

Crawford, W. R.: Energy flux and generation of diurnal shelf waves along Vancouver Island, J. Phys. Oceanogr., 14, 1600 – 1607, https://doi.org/10.1175/1520-0485(1984)014<1600:EFAGOD>2.0.CO;2, 1984.

Copernicus marine database: web source http://marine.copernicus.eu/services-portfolio/access-to-products/?option=com_csw&view=details&product_id=NORTHWESTSHELF_ANALYSIS_FORECAST_PHY_004_013, last access 18.09.19

Danilov, S. and Androsov, A.: Cell-vertex discretization of shallow water equations on mixed unstructured meshes, Ocean Dynam., 65, 33 – 47, https://doi.org/10.1007/s10236-014-0790-x, 2015.

Danilov, S., Sidorenko, D., Wang, Q., and Jung, T.: The Finite-volumE Sea ice–Ocean Model (FESOM2). Geosci. Model Dev., 10, 765 – 789, https://doi.org/10.5194/gmd-10-765-2017, 2017.

Dronkers, J.: Tidal asymmetry and estuarine morphology, Neth. J. Sea Res., 20, 117 – 131, https://doi.org/10.1016/0077-7579(86)90036-0, 1986

Egbert, G. D. and Erofeeva, S. Y.: Efficient inverse modeling of barotropic ocean tides. J. Atmos. Ocean. Tech., 19, 183 – 204, https://doi.org/10.1175/1520-0426(2002)019<0183:EIMOBO>2.0.CO;2, 2002.

Friedrichs, C. T. and Aubrey, D. G.: Non-linear tidal distortion in shallow well-mixed estuaries: a synthesis, Estuar. Coast. Shelf S., 27, 521 – 545, https://doi.org/10.1016/0272-7714(88)90082-0, 1988.

Gätje, C. and Reise, K. (Eds.): Ökosystem Wattenmeer: Austausch-, Transport- und Stoffumwandlungsprozesse, Springer, Berlin, Heidelberg, Germany, https://doi.org/10.1007/978-3-642-58751-1, 1998.

Gräwe, U., Burchard, H., Müller, M. and Schuttelaars, H. M.: Seasonal variability in M2 and M4 tidal constituents and its implications for the coastal residual sediment transport, Geophys. Res. Lett., 41, 5563 – 5570, https://doi.org/10.1002/2014GL060517, 2014.

Gräwe, U., Flöser, G., Gerkema, T., Duran-Matute, M., Badewien, T. H., Schulz, E. and Burchard, H.: A numerical model for the entire Wadden Sea: Skill assessment and analysis of hydrodynamics, J. Geophys. Res-Oceans, 121, 5231 – 5251, https://doi.org/10.1002/2016JC011655, 2016.

Gurvan, M., Bourdallé-Badie, R., Bouttier, P-A., Bricaud, C, Bruciaferri, D., Calvert, D., Chanut J., Clementi, E., Coward, A., Delrosso, D., Ethé, C., Flavoni, S., Graham, T., Harle, J., Iovino, D., Lea, D., Lévy, C., Lovato, T., Martin, N., Masson, S., Mocavero, S., Paul, J., Rousset, C., Storkey, D., Storto, A. and Vancoppenolle, M.: NEMO ocean engine (Version v3.6), Notes du Pôle de Modélisation de L'institut Pierre-Simon Laplace (IPSL), Zenodo, http://doi.org/10.5281/zenodo.1472492, 2017.

Hayes, M. O.: General morphology and sediment patterns in tidal inlets, Sediment. Geol., 26, 139 – 156, https://doi.org/10.1016/0037-0738(80)90009-3, 1980.

Kappenberg, J., Fanger, H., and Müller, A.: Currents and suspended particulate matter in tidal channels of the Sylt-Rømø Basin, Senck. Marit., 29, 93 – 100, https://doi.org/10.1007/BF03043947, 1998.

Kowalik, Z. and Proshutinsky, A. Y.: Diurnal tides in the Arctic Ocean, J. Geophys. Res., 98, 16449 – 16468, https://doi.org/10.1029/93JC01363, 1993.

Kuznetsov, I., Androsov, A., Fofonova, V., Danilov, S., Rakowsky, N., Harig, S., and Wiltshire, K. H.: 3D dynamics of the Southeastern North Sea, effects of variable resolution, Ocean Sci. Discuss., https://doi.org/10.5194/os-2019-103, in review, 2019.

Lumborg, U. and Pejrup, M.: Modelling of cohesive sediment transport in a tidal lagoon — an annual budget, Mar. Geol., 218, 1-16, https://doi.org/10.1016/j.margeo.2005.03.015, 2005.

Lumborg, U. and Windelin, A.: Hydrography and cohesive sediment modelling: Application to the Rømø Dyb tidal area, J. Marine Syst., 38, 287 – 303, https://doi.org/10.1016/S0924-7963(02)00247-6, 2003.

Mielck, F., Hass, H.C., Betzler, C.: High-Resolution Hydroacoustic Seafloor Classification of Sandy Environments in the German Wadden Sea, Journal of Coastal Research, 30(6), 1107– 1117, 2014.

Müller, M.: The influence of changing stratification conditions on barotropic tidal transport and its implications for seasonal and secular changes of tides, Cont. Shelf Res., 47, 107 – 118, https://doi.org/10.1016/j.csr.2012.07.003, 2012.

Müller, M., Cherniawsky, J. Y., Foreman, M. G. G. and von Storch, J.-S.: Seasonal variation of the M2 tide, Ocean Dynam., 64, 159 – 177, https://doi.org/10.1007/s10236-013-0679-0, 2014.

Nortier, R. J.; Morphodynamics of the Lister Tief tidal basin. M. S. thesis, TU Delft, Netherlands, pp. 76, available at: http://resolver.tudelft.nl/uuid:89da7250-9acb-429d-bb71-d7dbc60e7755, 2004.

Oost, A. P., van Buren, R. and Kieftenburg, A.: Overview of the hydromorphology of ebb-tidal deltas of the trilateral Wadden Sea, Deltares, Netherlands, Deltares report 11200926-000, pp. 334, 2017.

Pawlowicz, R., Beardsley, B. and Lentz, S.: Classical tidal harmonic analysis including error estimates in MATLAB using T_TIDE, Computat. Geosci., 28, 929 – 937, https://doi.org/10.1016/S0098-3004(02)00013-4, 2002.

Pejrup, M., Larsen, M. and Edelvang, K.: A fine-grained sediment budget for the Sylt-Rømø tidal basin, Helgolander Meeresun., 51, 253 – 268, https://doi.org/10.1007/BF02908714, 1997.

Postma, H.: Sediment transport and sedimentation in the estuarine environment, in: Estuaries, edited by: Lauff, G. H., American Association for the Advancement of Science, Washington, DC, 158 – 179, 1967.

Postma, H.: Exchange of materials between the North Sea and The Wadden Sea, Marine Geology, 40, 99–213, 1981.

Purkiani, K., Becherer, J., Flöser, G., Gräwe, U., Mohrholz, V., Schuttelaars, H. M. and Burchard, H.: Numerical analysis of stratification and destratification processes in a tidally energetic inlet with an ebb tidal delta, J. Geophys. Res-Oceans, 120, 225– 243, https://doi.org/10.1002/2014JC010325, 2015.

Purkiani, K., Becherer, J., Klingbeil, K. and Burchard, H.: Wind-induced variability of estuarine circulation in a tidally energetic inlet with curvature, J. Geophys. Res-Oceans, 121, 3261 – 3277, https://doi.org/10.1002/2015JC010945, 2016.

Ruiz-Villarreal, M., Bolding, K., Burchard, H. and Demirov, E.: Coupling of the GOTM turbulence module to some three dimensional ocean models, in: Marine Turbulence: Theories, Observations and Models, edited by: Baumert, H. Z., Simpson J., and Sündermann J., Cambridge University Press, Cambridge, United Kingdom, 225 – 237, 2005.

Salomon, J.-C. and Allen, G.-P.: (Effects of tides on sedimentology in estuaries with large tide ranges), [Role sedimentologique de la mare dans les estuaires a fort marnage], Compagnie Francais des Petroles, Notes et Memoires 18, 35 – 44, 1983.

Sander, L., Amorim, F. L. L, Fofonova, V., Hass, H. C.: Tidal geomorphology and spatial dynamics of primary bedforms in a complex microtidal catchment in the northern Wadden Sea, in preparation, 2019.

Stanev, E. V., Al-Nadhairi, R., and Valle-Levinson, A.: The role of density gradients on tidal asymmetries in the German Bight, Ocean Dynam., 65, 77 – 92, 2015.

Stanev, E. V., Schulz-Stellenfleth, J., Staneva, J., Grayek, S., Grashorn, S., Behrens, A., Koch, W. and Pein, J.: Ocean forecasting for the German Bight: From regional to coastal scales. Ocean Sci., 12, 1105 – 1136, https://doi.org/10.5194/os-12-1105-2016, 2016.

Thompson, J. F.: Elliptic grid generation, Appl. Math. Comput., 10 – 11, 79 – 105, https://doi.org/10.1016/0096-3003(82)90188-6, 1982.

Umlauf, L. and Burchard, H.: Second-order turbulence closure models for geophysical boundary layers. A review of recent work, Cont. Shelf. Res., 25, 795 – 827, https://doi.org/10.1016/j.csr.2004.08.004, 2005.

Valerius, J., Feldmann, J., van Zoest, M. Milbradt P. and Zeiler, M.: Documentation of sedimentological products from the AufMod project Functional Seabed Model, data format: Text files (CSV, XYZ), Federal Maritime and Hydrographic Agency (BSH) and smile consult GmbH, Germany, unpublished report, available at: ftp://ftp.bsh.de/outgoing/AufMod-Data/CSV_XYZ_files/DocumentationSedimentologyCSV_EN.pdf, 2013.

Voltzinger, N. E and Androsov, A. A.: Simulation of the energy of barotropic–baroclinic interaction in the Strait of Bab el Mandeb (the Red Sea), Izv. Atmos. Ocean. Phy+, 44, 121 – 137, https://doi.org/10.1134/S0001433808010143, 2008.

Werner, S. R., Beardsley, R. C. and Williams, A. J. Bottom friction and bed forms on the southern flank of Georges Bank, J. Geophys. Res., 108, 8004, https://doi.org/10.1029/2000JC000692, 2003.

Werum Software & Systems CIS AG: DSHIP V3. User Manual. Version 1.4, User Manual, available at: http://dship-alkor.geomar.de/dship-usermanual/dship-user-manual_en.pdf, 2016.

Woodworth, P. L., Shaw, S. M. and Blackman, D. L.: Secular trends in mean tidal range around the British Isles and along the adjacent European coastline, Geophys. J. Int., 104, 593 – 609, https://doi.org/10.1111/j.1365-246X.1991.tb05704.x, 2007.

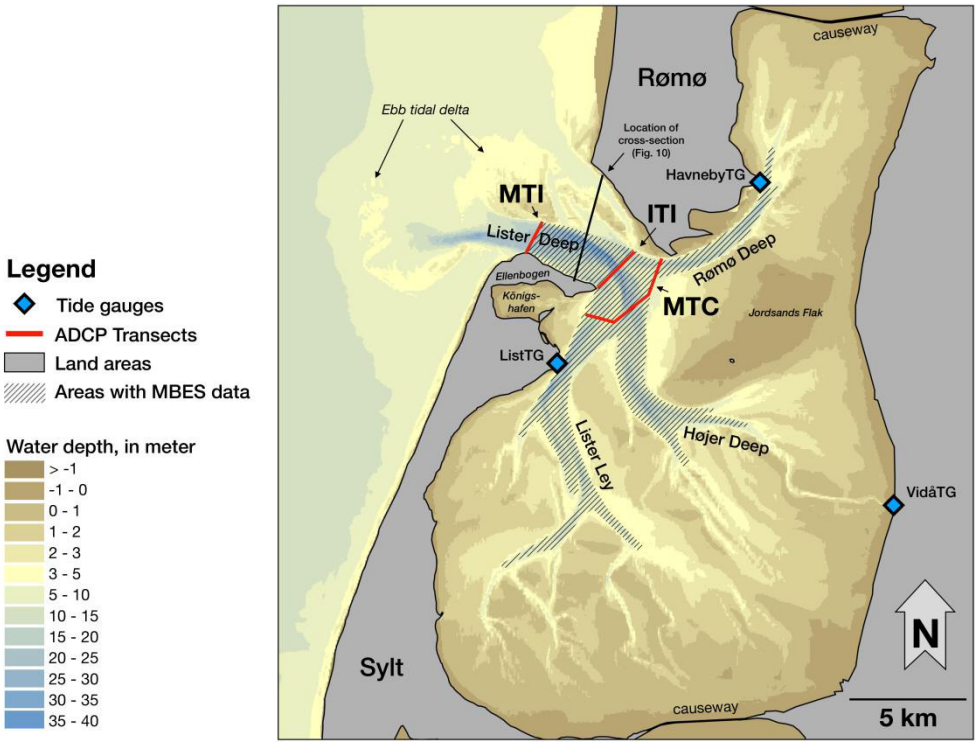

Figure 1. The bathymetry of the considered domain. The red lines indicate ADCP transects, the blue rhombuses show positions of the tide gauges. The hatched area represents zone with the recent multibeam echo sounder (MBES) data.

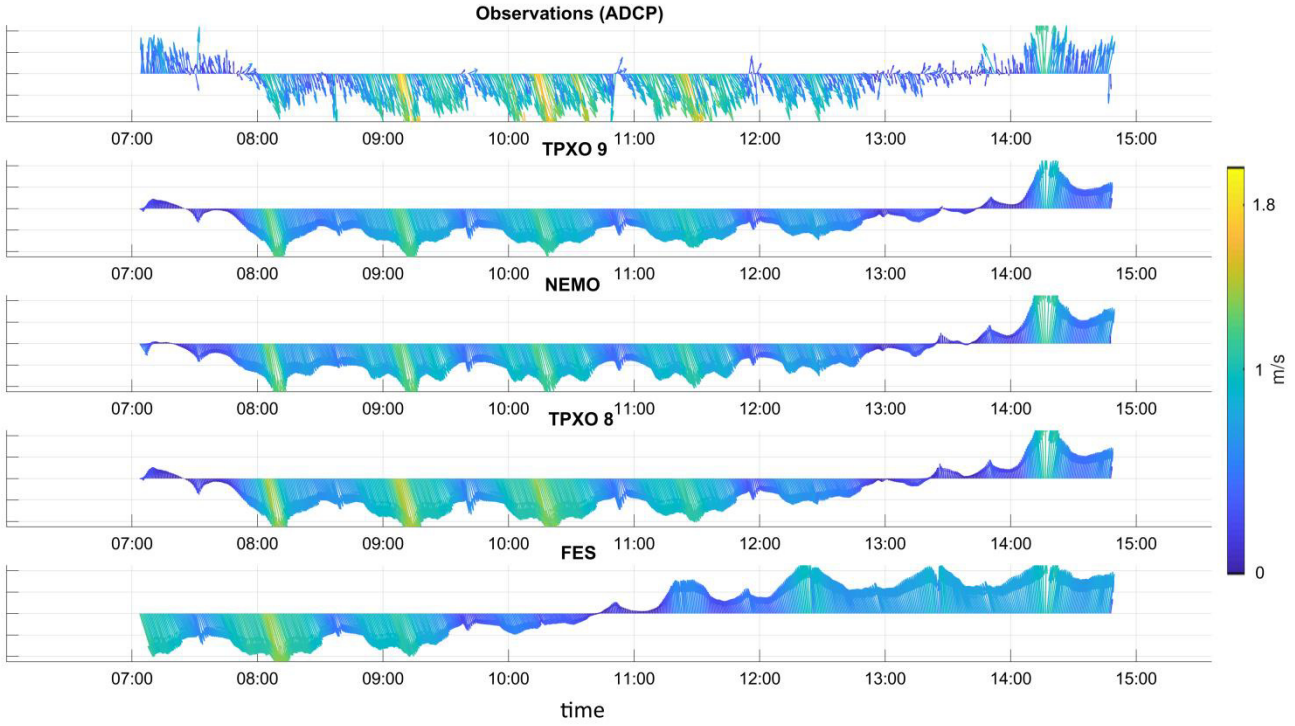

Figure 2. The observed and modelled depth-averaged velocities on May 29, 2018. The arrow color indicates the current magnitude [m/s]; arrow directions indicate the current direction.

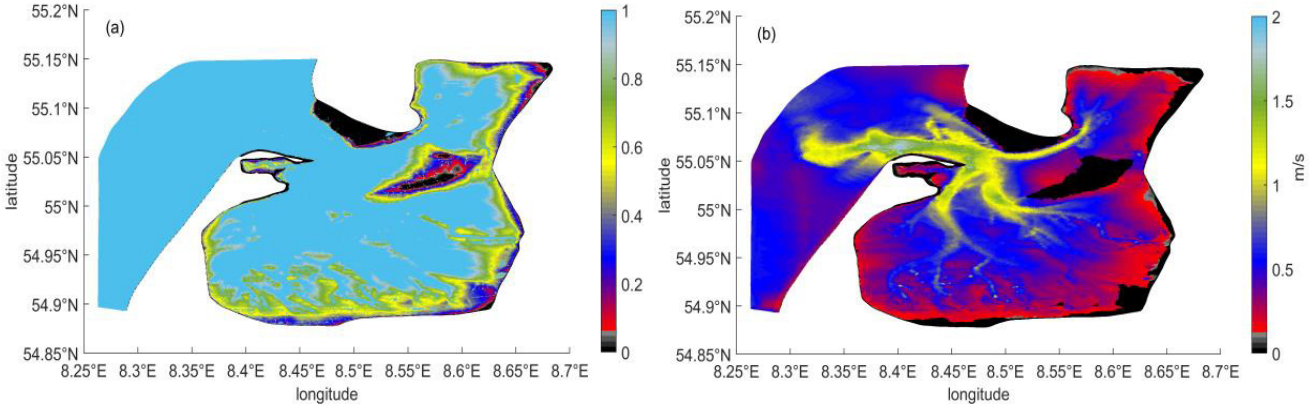

1220

Figure 3. a) The probability of wetting based on simulations of the two full tidal cycles using the unstructured grid. b) The peak tidal velocities at the current position using the unstructured grid.

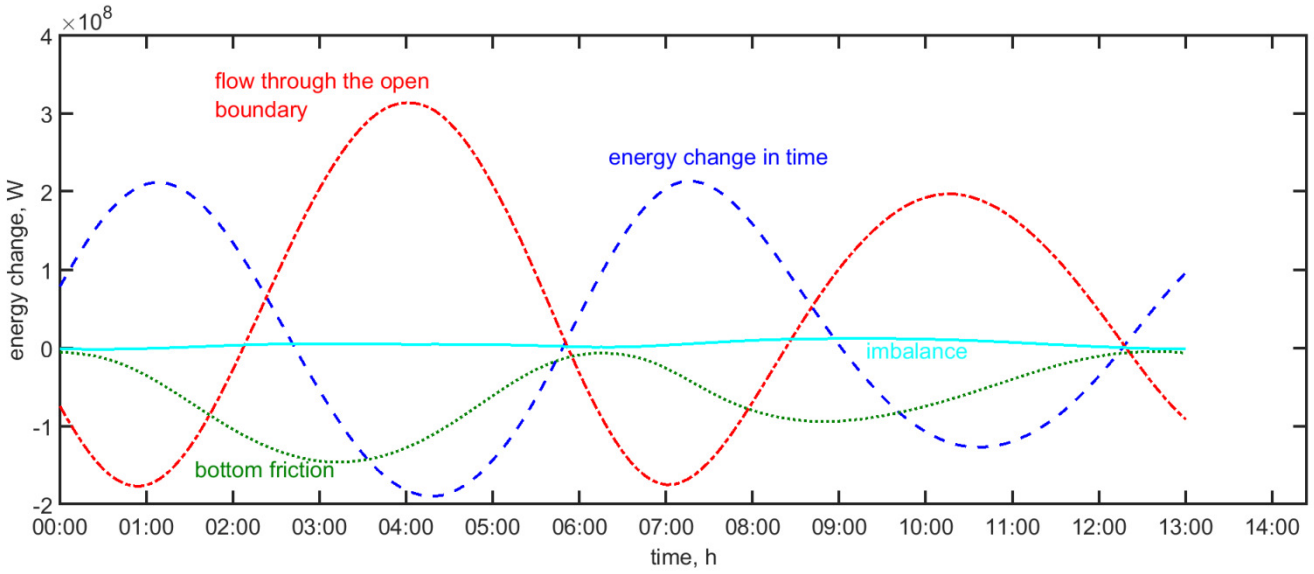

1225 **Figure 4.** The energy budget for the depth-averaged solution with open boundary conditions from the TPXO 9 database for summary tide, [W], in blue (dashed line): energy change in time, in red (dash-dotted line): flow through the open boundaries, in green (dotted line): bottom friction, in cyan (solid line): imbalance.

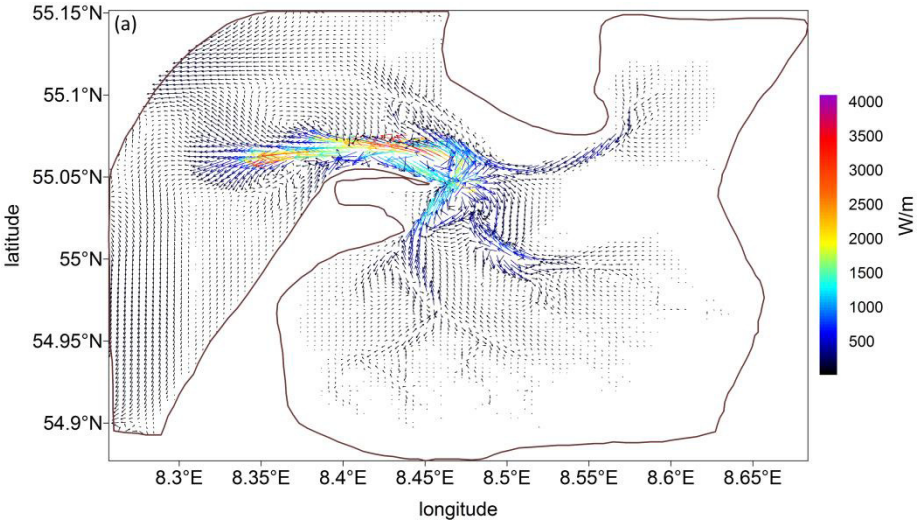
(a)
55.15°N
55.1°N
55.05°N
55°N
54.95°N
54.9°N
latitude
8.3°E
8.35°E
8.4°E
8.45°E
8.5°E
8.55°E
8.6°E
8.65°E
longitude
4000
3500
3000
2500
2000
1500
1000
500
W/m

1230

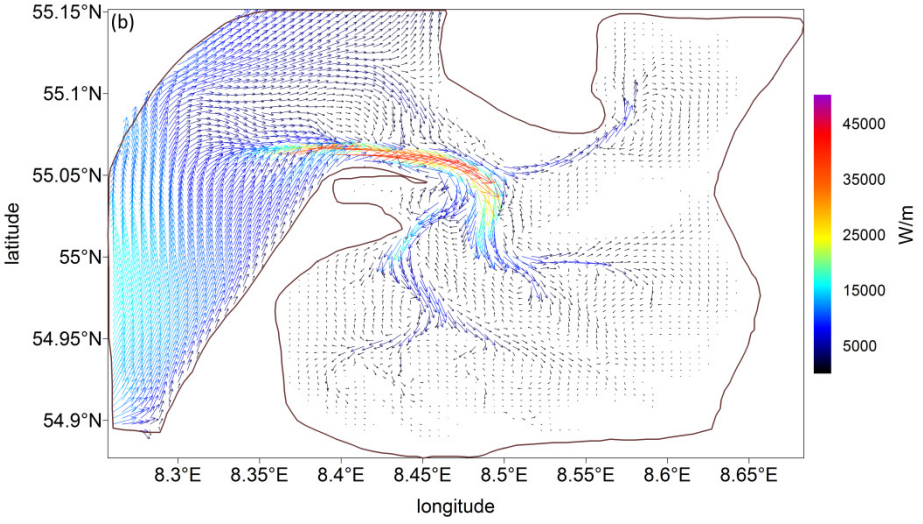
(b)
55.15°N
55.1°N
55.05°N
55°N
54.95°N
54.9°N
latitude
8.3°E
8.35°E
8.4°E
8.45°E
8.5°E
8.55°E
8.6°E
8.65°E
longitude
45000
35000
25000
15000
5000
W/m

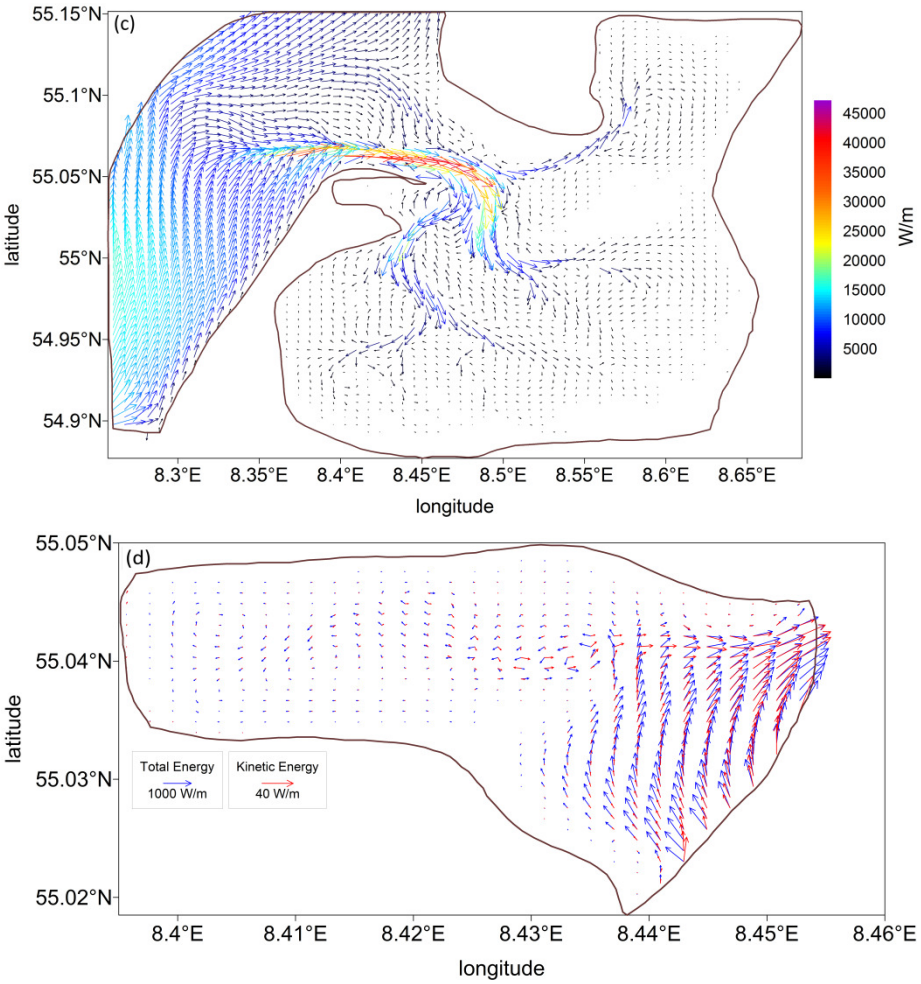

1235 **Figure 5.** The flux of tidal energy (summary tide): a) kinetic; b) potential; c) total ($\mathbf{E_\lambda}, \mathbf{E_\theta}$); d) the total (blue arrows) and kinetic (red arrows) energy fluxes for the Königshafen subarea. The potential energy fluxes behavior is visually identical to the total energy fluxes one.

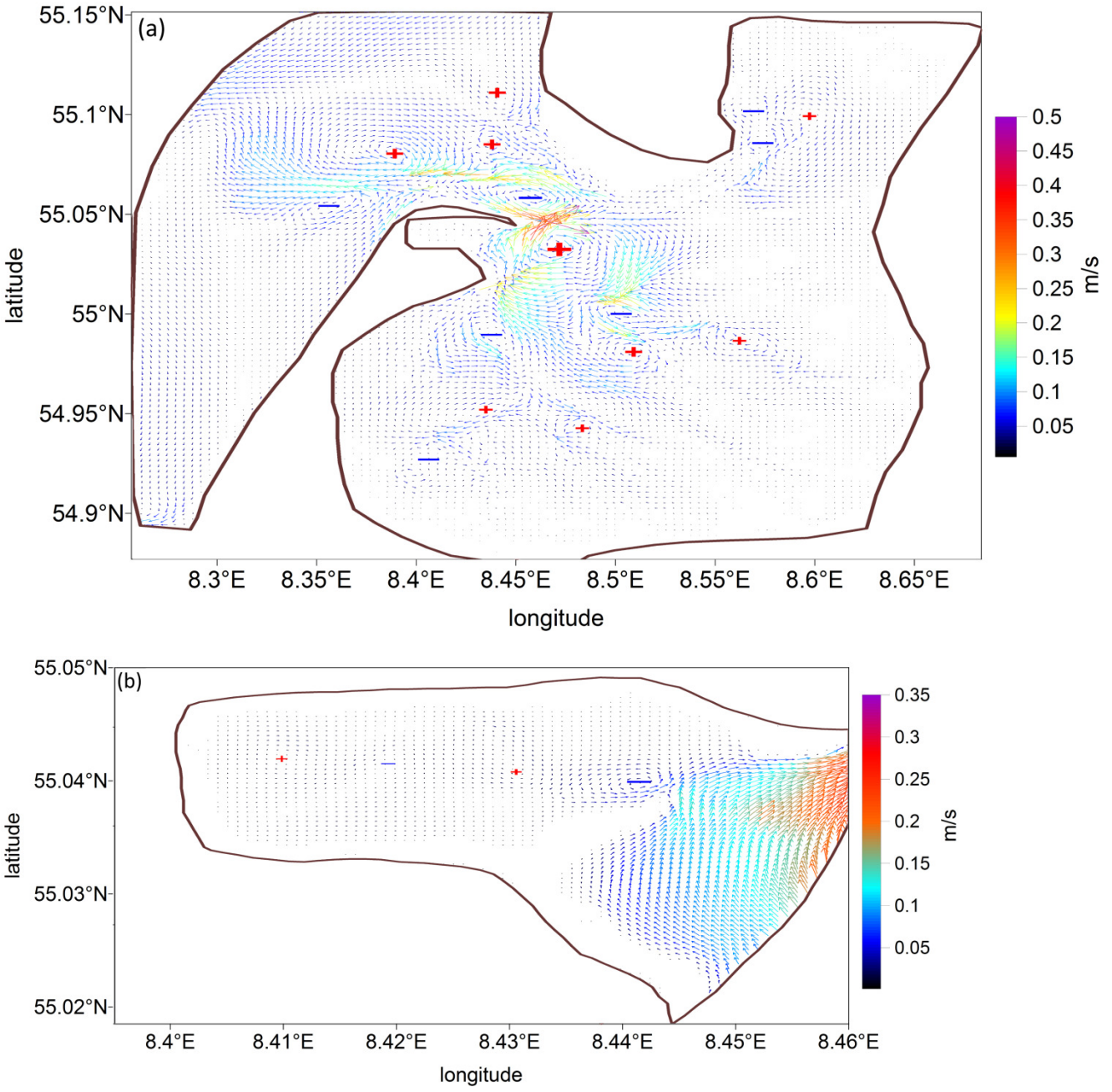

Figure 6. Residual circulation of the summary tide for: a) the whole area considered; b) the Königshafen embayment. The '+' and '-' illustrate the clockwise and counterclockwise rotation of the major gyres present in the system. The residual circulation is demonstrated on the unstructured grid.

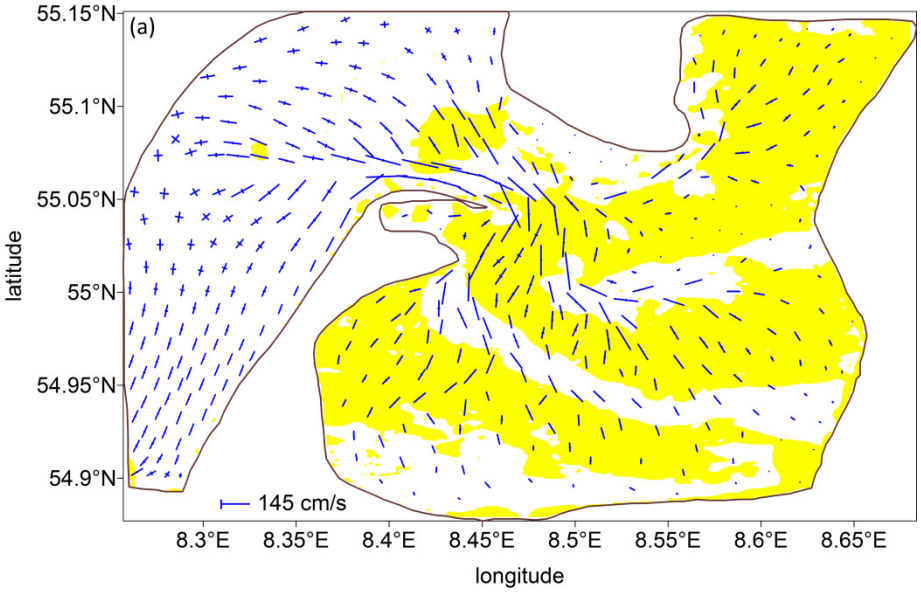
(a)
55.15°N
55.1°N
55.05°N
55°N
54.95°N
54.9°N
latitude
145 cm/s
8.3°E
8.35°E
8.4°E
8.45°E
8.5°E
8.55°E
8.6°E
8.65°E
longitude

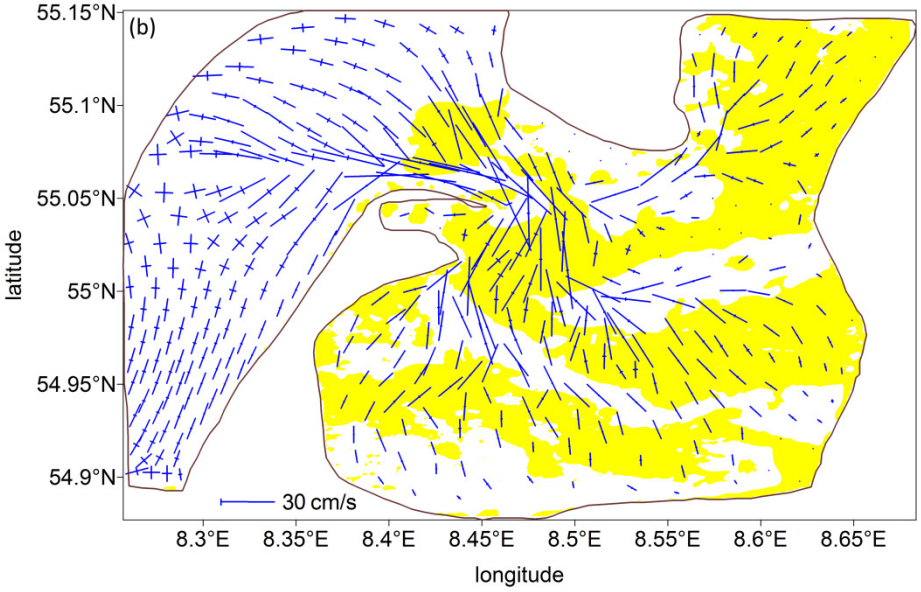
(b)
55.15°N
55.1°N
55.05°N
55°N
54.95°N
54.9°N
latitude
30 cm/s
8.3°E
8.35°E
8.4°E
8.45°E
8.5°E
8.55°E
8.6°E
8.65°E
longitude

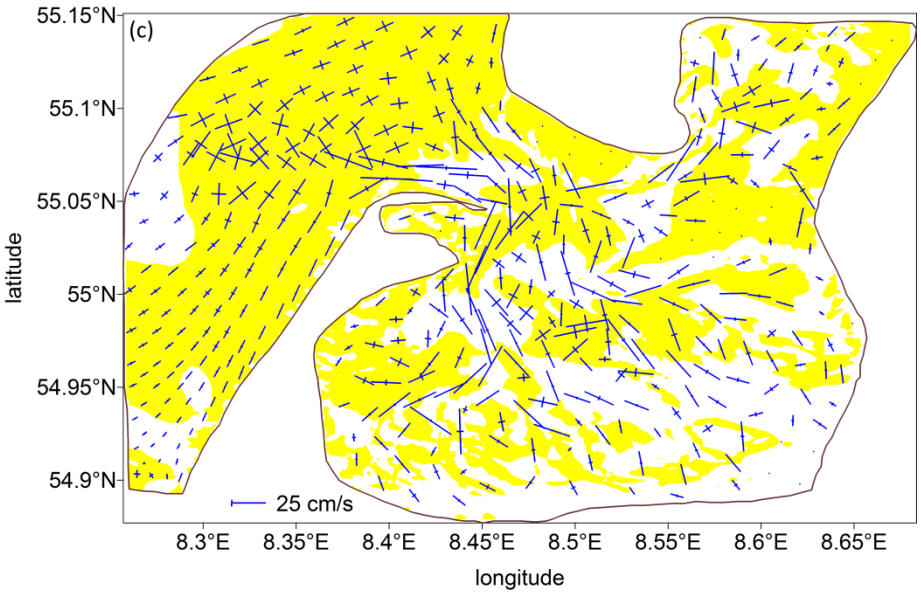

Figure 7. Axes of the a) M2, b) S2, c) M4 tidal current ellipses and zones of the minor-to-major axis ratios. Yellow zones denote the domain of anticyclonic rotation of the current vector.

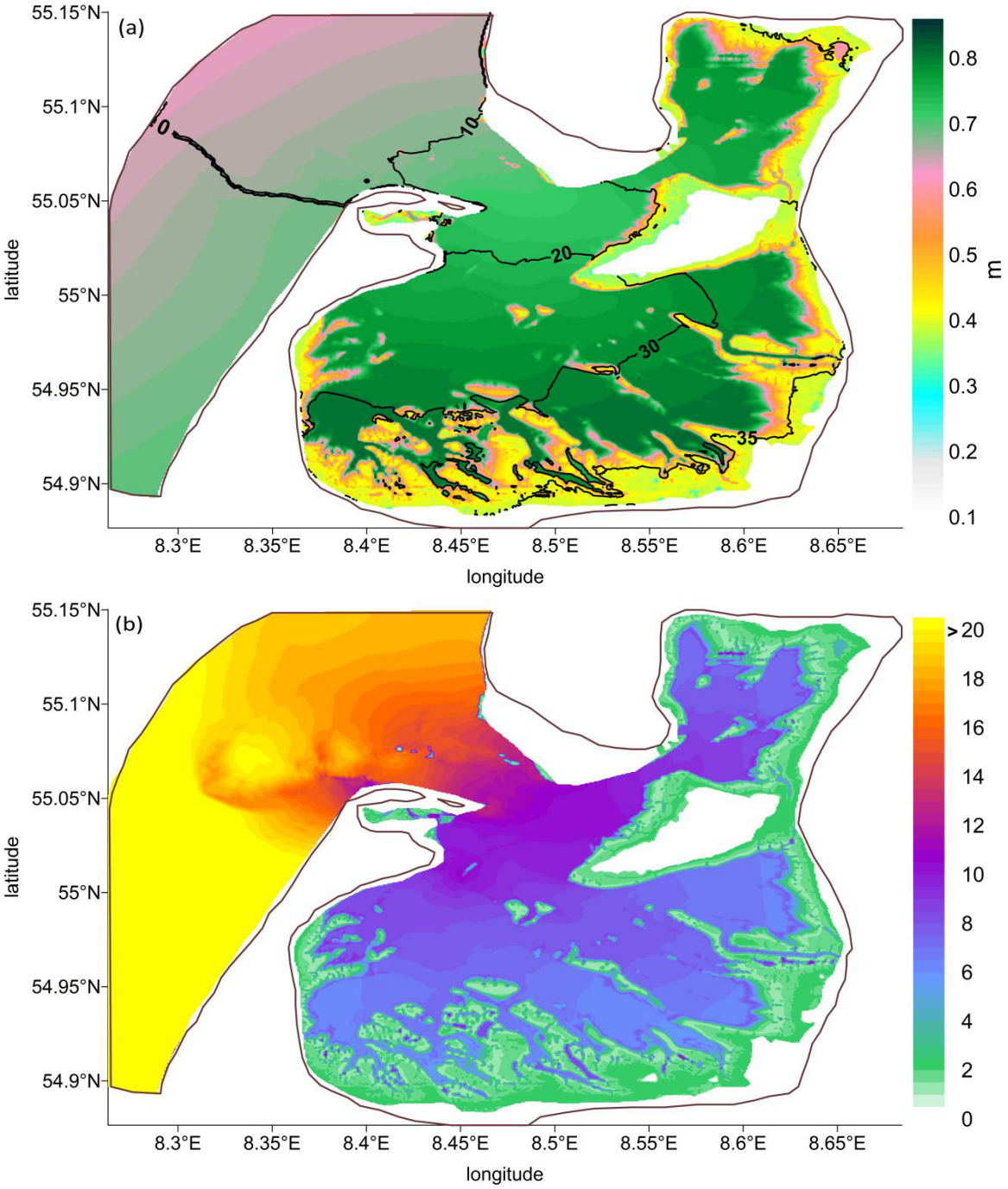

1255 **Figure 8**. a) The relative weight of the linearity: the ratio of M2 wave amplitude to the sum of the major nonlinear constituents. b) Tidal map for the M2 wave: phases, [°], are demonstrated via contour lines, amplitudes, [m], are via color

bar. The maps were created based on elevation data analysis. The white color indicates zone where topography features are above 0-sea level.

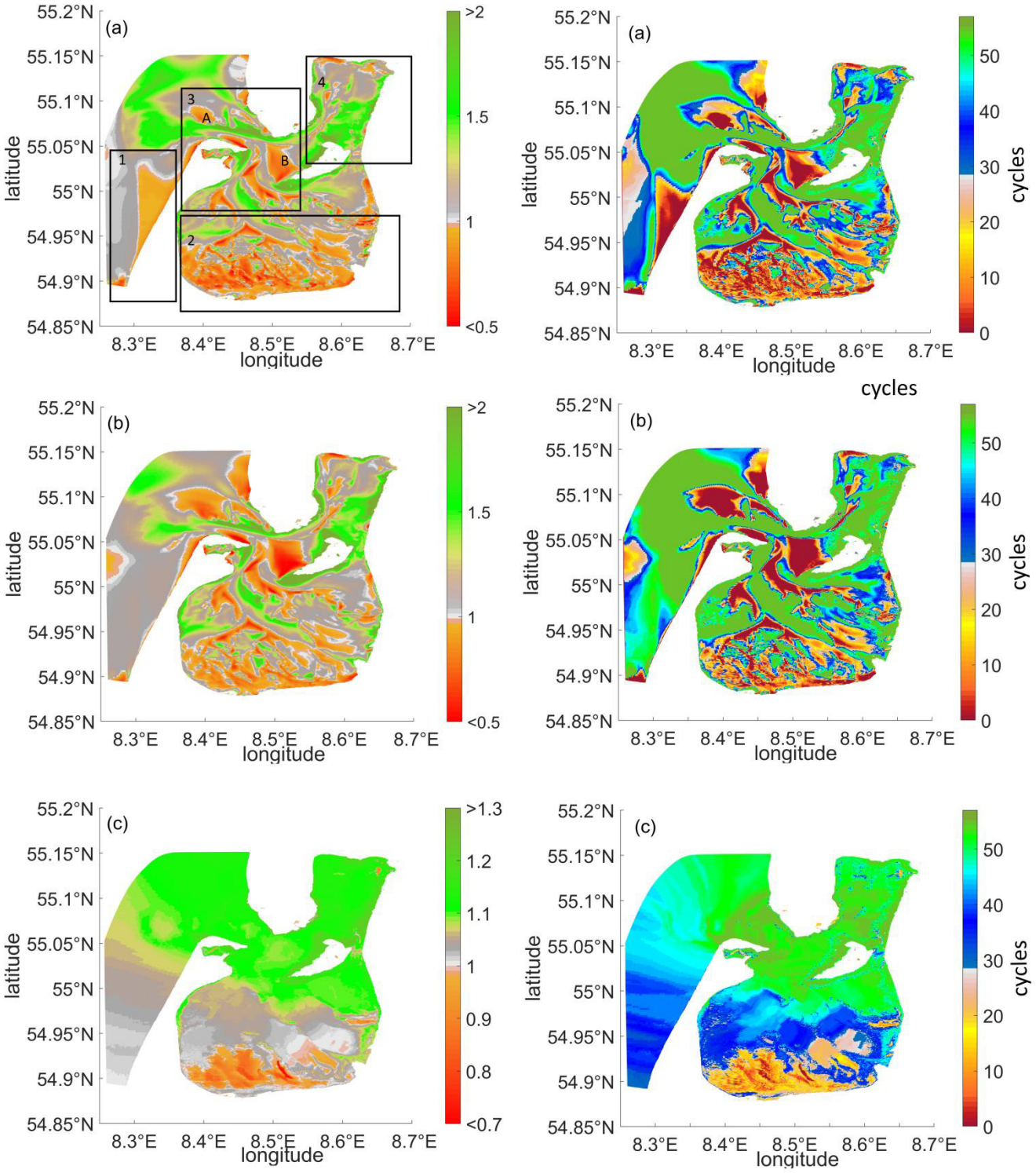
(a)
(b)
(c)
latitude
longitude
cycles
55.2°N
55.15°N
55.1°N
55.05°N
55°N
54.95°N
54.9°N
54.85°N
8.3°E
8.4°E
8.5°E
8.6°E
8.7°E
1
2
3
4
A
B
>2
1.5
1
<0.5
>1.3
1.2
1.1
0.9
0.8
<0.7
50
40
30
20
10
0

Figure 9. The ebb-flood dominance asymmetry maps. Left panel: ratio of a) maximum velocities during ebb and flood; b) mean velocities during ebb and flood; c) durations of flood and ebb. Right panel: frequency of event within a lunar (synodic) month (amount of the tidal cycles) a) maximum velocities during ebb are higher than during flood; b) mean velocities during ebb are higher than during flood; c) flood is longer than ebb. Numbers 1-4 indicate different zones under consideration. The A, B demonstrates an example of the subareas in which the strong flood dominance in terms of velocity does not mean shorter flood. Subareas which do not take part at least at one flood-ebb cycle are removed.

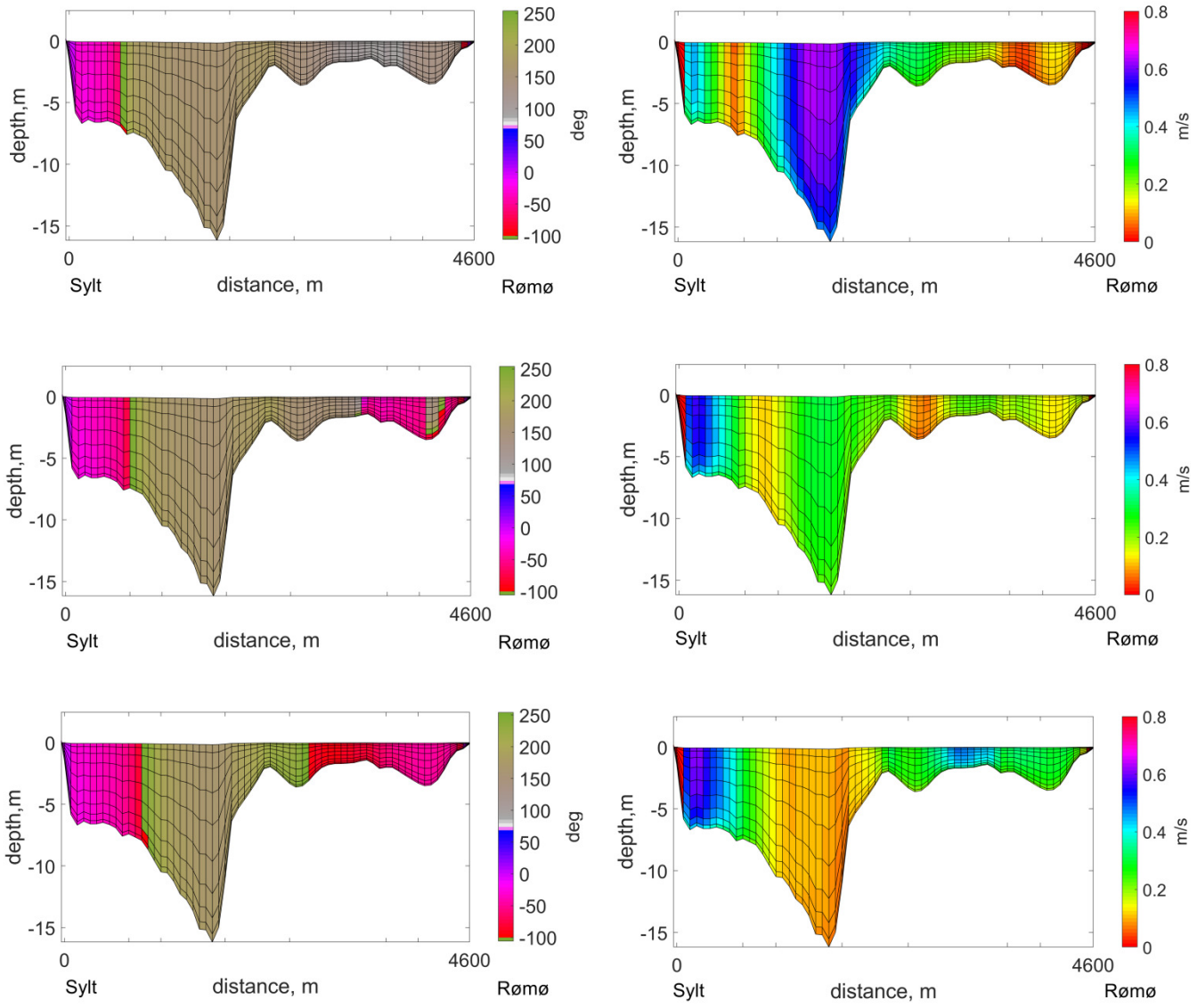

Figure 10. Snap-shots of direction relative to the y-axes (counted positively counterclockwise), [°], and magnitude [m/s] of velocities within the cross-section which connects Sylt (left shore) and Rømø (right shore); the angle between y-axes and the cross-section is -16° . In the left panel, the grey-green color indicates water outflow; blue-red color indicates water inflow. The snapshots capture the transition phase from ebb to flood with a 20-minute interval from one picture to another (top to bottom). The top panel is a snapshot of a moment when the external part of the domain is already at first-stage flood and the internal part of the domain is still at last-stage ebb.

Table 1. The summary of the five cruises on board of Research Vessel "Mya II" profiling three main transects: the Inner Tidal Inlet (ITI), the Main Tidal Channels (MTC) and the Outer Tidal Inlet (OTI).

Transect Name	**Date**	**Lon / Lat (°)** **(Start – End)**	**Tidal Period**	**Duration (h)**
ITI	22/05/2018	8.464 / 55.047 8.489 / 55.062	neap	6:28
MTC	23/05/2018	8.461 / 55.039 8.474 / 55.035	neap+1 day	6:19
	24/05/2018	8.499 / 55.046 8.505 / 55.056	neap+2 days	5:56
ITI	29/05/2018	8.464 / 55.047 8.489 / 55.062	spring	7:11
OTI	30/05/2018	8.418 / 55.059 8.428 / 55.071	spring+1 day	12:24

Table 2. The inter-comparison of the observed and simulated velocities based on different open boundary conditions in the area of Lister Deep. The table presents Root Mean Square Deviation (RMSD, m/s) and correlation coefficients (C.C.) for 'u' and 'v' velocity components. The results are given for the simulations performed on the curvilinear grid.

N of obs.	Date in May		FES2014	NEMO	TPXO8.1	TPX09	Mean vel., m/s (obs.)	Max vel., m/s (obs.)
655	**22**	**RMSD**	0.34	0.34	0.3	0.28	0.64	1.43
		C.C. u, v	0.84, 0.83	0.83, 0.83	0.84, 0.84	0.87, 0.85		
637	**23**	**RMSD**	0.32	0.35	0.31	0.31	0.55	1.56
		C.C. u, v	0.81, 0.82	0.78, 0.78	0.81, 0.82	0.82 0.82		
618	**24**	**RMSD**	0.41	0.32	0.34	0.31	0.54	1.31
		C.C. u, v	0.69, 0.5	0.83, 0.64	0.8, 0.62	0.84, 0.66		
764	**29**	**RMSD**	0.92	0.32	0.31	0.3	0.67	1.98
		C.C. u, v	0.09, 0.26	0.86, 0.84	0.86, 0.85	0.89, 0.87		
1259	**30**	**RMSD**	1	0.33	0.26	0.26	0.8	1.73
		C.C. u, v	0.18, 0.13	0.94, 0.76	0.97, 0.77	0.97, 0.76		

Table 3. Simulated and observed amplitudes, [cm], and phases, [°], of the major tidal constituents at different locations.

List TG						
	Curvilinear grid		**Unstructured grid**		**Observations**	
	Amp	**Phase**	**Amp**	**Phase**	**Amp**	**Phase**
M2	75.44	23.04	74.2	23.48	77.92	23.90
S2	17.12	85.01	19.34	95.83	18.92	94.55
N2	12.38	8.51	11.56	10.67	13.26	358.24
O1	6.74	277.2	6.77	276.81	8.33	269.30
K1	5.21	54.1	3.78	46.6	5.80	56.70
Q1	1.84	210.28	1.8	211.86	2.64	210.81
M4	4.92	188.68	3.89	181.43	5.08	214.86
RMSD: amp(cm)/ ph(°)	1.4 / 11.7		1.9 / 14.3			
Havneby TG						
	Curvilinear grid		**Unstructured grid**		**Observations**	
M2	76.23	24.21	75.26	24.91	79.83	24.78
S2	17.31	85.92	19.95	97.28	19.53	94.88
N2	12.49	9.23	11.87	11.95	13.42	359.15
O1	6.82	278.98	6.80	279.01	8.25	270.42
K1	5.26	56.12	3.80	50.54	5.90	62.26
Q1	1.83	211.65	1.80	213.16	2.85	211.03
M4	7.28	192.79	7.04	196.26	7.84	224.89

RMSD: **amp(cm)/** **ph(°)**	1.8 / 13.75		2.1 / 13.12			
Vidå TG						
	Curvilinear grid		**Unstructured grid**		**Observations**	
M2	67.74	35.94	65.71	37.21	63.41	42.35
S2	13.26	105.05	16.06	114.17	14.89	113.10
N2	9.82	29.47	8.91	31.19	9.78	18.30
O1	6.13	294.36	6	295.47	6.95	284.53
K1	4.9	73.47	3.59	71.78	5.58	79.42
Q1	1.19	223.36	1.25	224.92	1.78	217.68
M4	2.39	90.38	3.21	55.18	4.77	25.87
RMSD: **amp(cm)/** **ph(°)**	2 / 25.5		1.5 / 13.5			

1285